Electronic Supplementary Information (ESI) for Energy & Environmental Science

Coordinatively unsaturated nickel-nitrogen sites towards selective and high-rate CO_2 electroreduction

Chengcheng Yan, [‡a,b] ***Haobo Li,*** [‡a,b] ***Yifan Ye,*** [a,b] ***Haihua Wu,*** [a,b] ***Fan Cai,*** [a,b] ***Rui Si,*** [c] ***Jianping Xiao,*** [a] ***Shu Miao,*** [a] ***Songhai Xie,*** [d] ***Fan Yang,*** [a] ***Yanshuo Li,*** [e] ***Guoxiong Wang,**** [a] ***Xinhe Bao,**** [a]

[a] *State Key Laboratory of Catalysis, CAS Center for Excellence in Nanoscience, Dalian National Laboratory for Clean Energy, Dalian Institute of Chemical Physics, Chinese Academy of Sciences, Dalian, 116023.*

[b] *University of Chinese Academy of Sciences, Beijing, 100039, China.*

[c] *Shanghai Synchrotron Radiation Facility, Shanghai Institute of Applied Physics, Chinese Academy of Sciences, Shanghai, 201204, China.*

[d] *Shanghai Key Laboratory of Molecular Catalysis and Innovative Materials, Department of Chemistry, Fudan University, Shanghai, 200433, China.*

[e] *School of Material Science and Chemical Engineering, Ningbo University, Ningbo, 315211, China.*

‡ *These authors have contributed equally to this work.*

**Corresponding authors: G. Wang (wanggx@dicp.ac.cn), X. Bao (xhbao@dicp.ac.cn).*

1. Experimental Section

Materials and chemicals

Zinc nitrate hexahydrate ($Zn(NO_3)_2{\cdot}6H_2O$, >99%) and nickel nitrate hexahydrate ($Ni(NO_3)_2{\cdot}6H_2O$, >98%) and methanol (MeOH) were purchased from Sinopharm Chemical Reagent Co., Ltd (China). 2-Methyl imidazole (2-MeIM, 99%) was purchased from J&K Chemicals. Nafion solution (5 wt%) was purchased from Alfa Aesar. Nickel phthalocyanine (NiPc) was purchased from Sigma-Aldrich. All the reagents were used without further purification.

1.1 Material synthesis

Synthesis of Zn_xNi_y ZIF-8

Zn/Ni bimetallic zeolitic imidazolate framework-8 with different Zn/Ni ratios were prepared using a modified protocol according to the method of Li et al.[1] The obtained powder is denoted as Zn_xNi_y ZIF-8, where x/y means the molar ratio of Zn to Ni in the starting materials. Typically, certain amounts of $Zn(NO_3)_2{\cdot}6H_2O$ and $Ni(NO_3)_2{\cdot}6H_2O$ were first dissolved in methanol, then certain amount of 2-MeIM methanol solution was poured into the mixed metal nitrate solution and stirred at room temperature for 24 h. For all the samples, the molar ratio of metal ions to 2-MeIM remained as 1:8. Zn_xNi_y ZIF-8 nanocrystals were separated by centrifugation, thoroughly washed with methanol for three times and then dried under vacuum at room temperature overnight. Pure ZIF-8 was synthesized using the same method without the addition of $Ni(NO_3)_2$.

Synthesis of C-Zn_xNi_y ZIF-8

C-Zn_xNi_y ZIF-8 catalysts were obtained by one-step pyrolysis method. In a typical treatment, 0.4 g as-prepared Zn_xNi_y ZIF-8 was heated to 1000 ºC (or 900 ºC) at a rate of 3 ºC min^{-1} and kept at the desired temperature for 4 h (or 10 h) under the flowing Ar atmosphere in a horizontal quartz crucible, followed by naturally cooling down to room temperature. The pyrolysis products were denoted as C-Zn_xNi_y ZIF-8 and C-ZIF-8 (for pure ZIF-8 derived carbon material). To highlight the critical role of Ni species towards electrochemical CO_2 reduction reaction (CO_2RR), 0.4 g as-prepared

Zn_xNi_y was pyrolyzed at 900 °C for 4 h as described above to obtain additional three samples. The pyrolysis products were denoted as C-Zn_xNi_y ZIF-8 (900°C-4h).

1.2 Physicochemical characterization

X-ray diffraction (XRD) was performed using a PANalytical X'pert PPR diffractometer with a Cu Kα radiation source (λ=1.5418Å) at 40 kV and 40 mA at a scan rate of 5° min^{-1}. The contents of Ni and Zn in the catalysts were measured by inductively coupled plasma optical emission spectroscopy (ICP-OES; ICPS-8100, Shimadzu). Transmission electron microscopy (TEM) and High-resolution TEM (HRTEM) images were acquired by a JEM-2100 microscopy operated at an accelerating voltage of 200 kV. Scanning electron microscopy (SEM) images were acquired by a field emission SEM (FE-SEM, JSM-7800F) with an accelerating voltage of 3 kV. High-angle annular dark field-scanning transmission electron microscopy (HAADF-STEM) measurements were performed on JEM-ARM200F (JEOL, Japan, for high-resolution images) and Tecnai F20 G2S-Twin (FEI, USA, for low-resolution images). Energy dispersive X-ray spectroscopy (EDS) images were collected by Aztec X-Max 80T (Oxford Instrument, UK, for low-resolution images). X-ray photoelectron spectroscopy (XPS) measurements were performed on the Thermo Scientific ESCALAB 250Xi spectrometer using an Al Kα X-ray source and pass energy of 20 eV. The binding energies were calibrated using the C 1s feature located at 284.6 eV as the reference. Nitrogen adsorption/desorption was investigated by a Quantachrome Autosorb iQ2 system at 77 K, and specific surface areas of the catalysts were determined by the Brunauer–Emmett–Teller (BET) equation. The CO_2 adsorption isotherms were measured using an iSorb HP2 instrument (Quantachrome Instruments). Ultra-high-purity grade CO_2 (99.999%) were used for the adsorption measurements. The samples were outgassed at 0.001 Torr and 200 °C for 10 h prior to the measurements. The X-ray absorption spectroscopy (XAS) measurements at Ni K (E_0=8333 eV) and Zn K (E_0=9659 eV) edge were performed at BL14W1 beamline[2] of Shanghai Synchrotron Radiation Facility (SSRF) operated at 3.5 GeV under "top-up" mode with a constant current of 260 mA. The energy was calibrated accordingly to the absorption edge of pure Ni foil (or Zn foil). Athena and Artemis codes were used to extract the data and fit the profiles. For the X-ray absorption near edge structure (XANES) part, the experimental absorption coefficients as function of energies μ(E) were processed by background subtraction and normalization procedures, and reported as "normalized absorption". The chemical valence of Ni (or Zn) in the samples were determined by the comparison with the reference Ni and NiPc (or Zn and ZnPc). For the extended X-ray absorption fine structure (EXAFS) part, the Fourier transformed (FT) data in *R* space were analyzed by applying first-shell approximate model for Ni-N (or Zn-N) contribution. The passive electron factor S_0^2, was determined by fitting the experimental data on Ni foil (or Zn foil), and then fixed for future analysis of the measured samples. The parameters describing the electronic properties (e.g., correction to the photoelectron energy origin, E_0) and local structure environment including coordination number (CN), bond distance (R) and Debye-Waller (D.W, i.e. σ^2) factor around the absorbing atoms were allowed to vary during the fitting process.

1.3 CO_2 electroreduction measurements

Carbon paper (Toray TGP-H-060) coated with microporous layer was used as the substrate for preparing the porous electrode. Specifically, carbon black ink containing Vulcan XC-72R carbon black and polytetrafluoroethylene (PTFE, Sigma-Aldrich) was firstly painted onto the carbon paper to form a microporous layer and then calcined at 350 °C in muffle furnace. The carbon black loading was about 1.0 mg cm^{-2} and the PTFE content in the microporous layer was 15 wt%. The as-prepared catalyst and 5 wt% Nafion solution were ultrasonically suspended in a water/ethanol mixture to form a homogeneous catalyst ink. The catalyst ink was painted onto the microporous layer with a size of 4.2 cm × 2.2 cm and dried at 70 °C for more than 30 min. The catalyst loading was deduced from the increment of catalyst weight on the carbon paper measured by a balance (Mettler Toledo ME104E, a resolution of 0.1 mg) and the Nafion content in the catalyst layer was 10 wt%. Except for controlled-potential tests for NiPc and TOF determination, the catalyst loading was

2.0 ± 0.1 mg cm^{-2}. For electrode with NiPc (Ni content ~10.28 wt%), the catalyst loading was 1.06 mg cm^{-2}, in order to maintain the same Ni loading with C-Zn_1Ni_4 ZIF-8. For TOF determination, a lower loading (0.088 mg cm^{-2} for C-Zn_1Ni_4 ZIF-8 and 0.226 mg cm^{-2} for C-Zn_1Ni_1 ZIF-8, respectively, to guarantee the same Ni loading on the electrode) was used to make sure that all of the painted catalysts were involved in the CO_2RR. The catalyst layer was prepared as described above except that the size of the carbon paper coated with microporous layer is 6.0 cm×8.0 cm for decreasing the weighing error.

CO_2 electroreduction experiments were carried out in an H-cell separated by Nafion 115, as shown in Fig. S11. The carbon paper painted with the catalyst layer was cut into a size of 1.0 cm×2.0 cm acting as the working electrode. The Ag/AgCl and Pt wire were used as the reference electrode and counter electrode, respectively, as reported in our previous work[3]. The potentials were controlled by an Autolab potentiostat/galvanostat (PGSTAT 302N). All potentials in this study were measured against the Ag/AgCl reference electrode and converted to the RHE reference scale using $E\ (\text{vs. RHE}) = E\ (\text{vs. Ag/AgCl}) + 0.21\ \text{V} + 0.0591 \times \text{pH}$.

CO_2 electroreduction performances were tested in CO_2-saturated 1 M $KHCO_3$ (or 0.5 M $KHCO_3$ and 0.1 M $KHCO_3$) solution at room temperature and under atmospheric pressure. The electrolyte volume for both anodic and cathodic compartments was 45 mL and magnetic stirrer was used to accelerate the mass transfer at a rotation rate of ~2500 rpm in the cathodic compartment. The electrolyte in both compartments was purged with 5% N_2/CO_2 (pure CO_2 for anodic compartment) at 20 mL min^{-1} for at least 30 min before each controlled-potential electrolysis. The gas products of CO_2 electroreduction were detected by an on-line micro gas chromatography (GC) (Agilent 490) equipped with a TCD detector and Molsieve 5A column once every four minutes. Argon was used as the carrier gas and nitrogen was the internal standard gas. CO and H_2 are the only detected gas products. Quantification of the products was obtained by the relative correction factor (R_{CO}=1.05, R_{H2}=0.084) derived from the calibration process. The liquid products were analyzed on a Bruker AVANCE III 400MHz nuclear magnetic resonance (NMR) spectrometer with 1-Propanesulfonic acid 3-(trimethylsilyl) sodium salt (DSS) as the internal standard and no liquid products were detected by NMR spectrometer.

The Faradaic efficiency was calculated using the following equation:

$$f_i = \frac{Q_i}{Q_{total}} = \frac{N_i \cdot n \cdot F}{Q_{total}}$$

where,

Q_{total}: the charge passed, C;

Q_i: the charge used for the reduction of certain product, C;

N_i: the number of moles for a specific product (measured by GC), mol;

n: the number of electrons exchanged for product formation, which is 2 for CO and H_2;

F: Faradaic constant, which is 96485 C mol^{-1}.

The sum of the Faradaic efficiencies for CO and H_2 production in this work were close to 100% with minor fluctuations(±5%) as shown in Fig. S15 and Table S7, due to bubbles sticking to the electrode surface and small uncertainties in quantification. Thus the total Faradaic efficiencies for each run were normalized to 100% to correct these fluctuations.[4] Each catalyst was tested for three times in parallel and the derived error bars were shown in related figures showing good reproducibility.

TOF for CO production was calculated as follow:

$$\text{TOF}(hr^{-1}) = \frac{I_{CO}/nF}{m_{cat} \times w/M_{Ni}} \times 3600$$

where

I_{CO}: partial current density for CO production, A;

n: the number of electron transferred for CO production, which is 2 for CO;

F: Faradaic constant, 96485 C mol^{-1};

m_{cat}: the mass of catalyst on the electrode, g;

w: Ni loading in the catalyst;

$M_{Ni} = 58.69\ g\ mol^{-1}$, atomic mass of Ni.

The stability test of C-Zn_1Ni_4 ZIF-8 catalyst for CO_2 electroreduction was performed at −0.63 V (vs. RHE) for 720 min under the same reaction conditions as described above (CO_2-saturated 1 M $KHCO_3$ solution), except that Tokuyama A201 anion exchange membrane was used instead of Nafion 115 cation exchange membrane in order to eliminate the concentration variation of $KHCO_3$ solution at the anodic and cathodic compartments during the stability test. After the stability test, the used electrode was washed with deionized water, and dried at room temperature overnight. Some catalysts was removed from the used electrode and dispersed in ethanol for TEM and HRTEM measurements. The other part of the used electrode was used for XPS and XAS measurements.

1.4 Estimation of diffusion layer thickness

In order to obtain the diffusion layer thickness under our CO_2RR test condition (in H-cell with a stirring rate of ~2500 rpm), we modified the H-cell as shown in Fig. SE1. A rotating glassy carbon (GC) disk electrode (Φ=5 mm) was used as the working electrode and immersed into the electrolyte solution at a similar position of the carbon paper during the CO_2RR measurements. 6.0 mg of the commercial 40 wt% Pt/C (Tanaka Kikinzoku Kogyo K. K., Japan) was premixed with 0.3 mL deionized water, 1.7 mL ethanol and 50 μL 5 wt% Nafion solution by ultrasonication for at least 1 h to form a homogeneous catalyst ink. Then 15 μL of the catalyst ink was dropwise deposited on the GC electrode with a Pt loading of 89.5 μg cm^{-2}. The electrolyte is deaerated 0.1 M NaOH aqueous solution with 10 mM $K_3Fe(CN)_6$. The current-potential curves with different rotation rates (400, 900, 1600, 2000, 2500, 3000 rpm) were measured at a scan rate of 10 mV s^{-1} in the positive sweep direction from 0.2 to 1.4 V vs. reversible hydrogen electrode (RHE) and are shown in Fig. SE2a. The current-potential curve under our CO_2RR test condition (in H-cell with a stirring rate of ~2500 rpm) was also measured similarly. Furthermore, the measured limiting currents were plotted against the square root of the rotation rate as shown in Fig. SE2b. The limiting current increases linearly with the square root of the rotation rate (with a slope of 0.0238) and the line intercepts the vertical axis near zero, which agrees well with the Levich equation $i_{l,c} = 0.62\mathrm{nFA}D_O^{2/3}\omega^{1/2}\upsilon^{-1/6}C_O^*$, confirming the validation of our system.

Herein,

$i_{l,c}$ is the Levich current, i.e. limiting cathodic current (A).

n is the number of moles of electrons transferred in the half reaction (number).

F is the Faraday constant, 96485 C mol^{-1}.

A is the electrode area, 0.1963 cm^2 for a GC electrode with a diameter of Φ=5 mm.

D_O is the diffusion coefficient of the oxidized form, for $Fe(CN)_6^{3-}$, Do ≈0.6×10^{-5} cm^2 s^{-1} at 20 °C. [5]

ω is angular frequency of rotation; $2\pi \times \text{rotation rate}$ (s^{-1}).

υ is kinematic viscosity, for H_2O, it is 0.01 cm^2 s^{-1}.

C_O^* is the bulk concentration of the oxidized form.

As shown in Fig.SE2a, the current-potential curve and limiting current under our CO_2RR test condition coincides with that at a rotation rate of 2000 rpm in the rotation disk electrode configuration, suggesting that the stirring is nearly equal to a rotation rate of 2000 rpm. Using this value, we can calculate the diffusion layer thickness according to the following equation:

$$\delta_{CO_2} = 1.61 D_{CO_2}^{1/3} \omega^{-1/2} \upsilon^{1/6}$$

δ_{CO_2} is the diffusion layer thickness for CO_2.

The diffusion layer thickness is calculated to be ~14.0 μm (taking the value of $D_{CO_2} = 2\times10^{-5}\ cm^2 s^{-1}$, rotation rate = 2000 rpm, $\upsilon = 0.01\ cm^2 s^{-1}$) , indicating that the stirring at ~2500 rpm inside the H-cell for CO_2RR measurements is sufficient to achieve a thinner diffusion layer. Then the limiting CO current density for CO_2RR (assuming that CO_2RR is only limited by the mass-transfer of dissolved CO_2 in aqueous electrolyte) is calculated to be ~94 mA cm^{-2} according to the following equation:

$$j_{l,c} = \frac{i_{l,c}}{A} = \frac{nFD_{CO_2}C_{CO_2}^*}{\delta_{CO_2}}$$

$j_{l,c}$ is the limiting cathodic current density (A/cm^2). The solubility of CO_2 ($C_{CO_2}^*$) in diluted aqueous electrolyte at 1atm is 34 mM, which is equivalent to 3.4×10^{-5} mol cm^{-3}.[6]

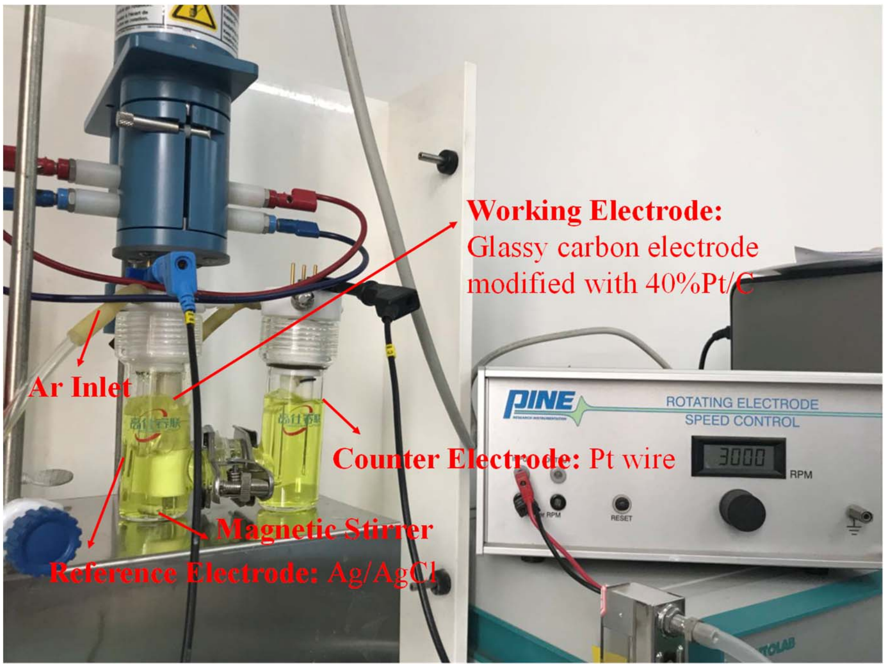

Fig. SE1. Picture of the detailed setup for the determination of the diffusion layer thickness.

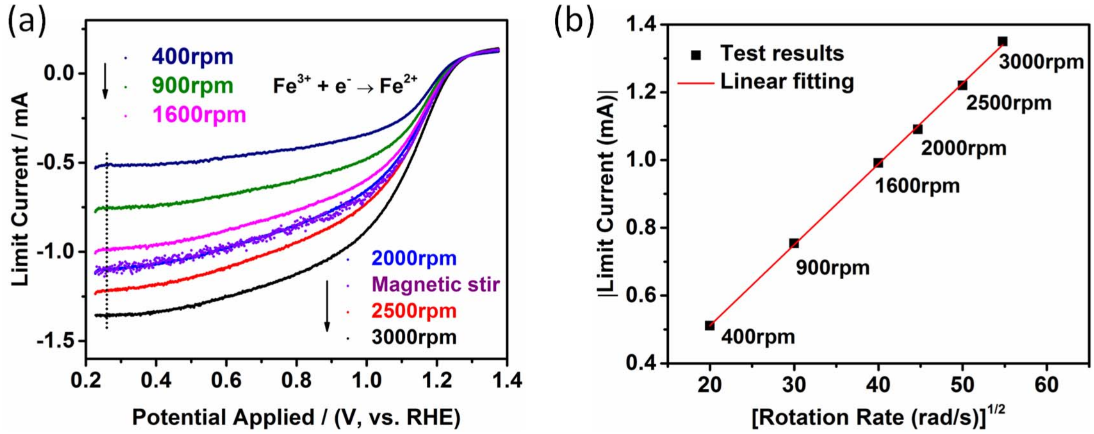

Fig. SE2. (a) Current-potential curves measured at different rotation rates; (b) The Levich plot at various rotation rates.

2. DFT calculations

DFT calculations have been performed using the Vienna *ab* initio simulation package (VASP)[7] with the projector-augmented wave (PAW)[8] method. All calculations were based on the same generalized gradient approximation (GGA) method with Perdew-Burke-Ernzerhof (PBE)[9] functional for the exchange-correlation term. The plane wave cutoff was set to 400 eV. The Brillouin zone integration was carried out with 2×2×1 Monkhorst-Pack[10] *k*-point grid. The convergence of energy and forces were set to 1×10^{-4} eV and 0.05 eV $Å^{-1}$, respectively. A periodically repeated single-layer graphene model with Ni-N structures embedded in the in-plane matrix has been built to simulate the Ni-N-C catalysts with a unit cell size of 5×5 and a vacuum slab height of 17 Å. All atoms of the catalysts and adsorbates were fully relaxed during calculations. The entropic corrections and zero-point energy (ZPE) have been included with detailed data in Tables S14 and S15. The free energy of each species is calculated by: $G = E_{DFT} + ZPE + \int C_v dT - T\Delta S$, where E_{DFT} is the DFT-optimized total energy, ZPE is the zero-point vibrational energy, $\int C_v dT$ is the heat capacity, T is the temperature, and ΔS is the entropy. The implicit solvent stabilization of the adsorbates has also been applied as: 0.25 eV for *COOH, 0.1 eV for *CO and 0 eV for *H (in reference to the literature by Nørskov et al.[11]). The explicit correction has been made on the free energy for the effects of electrolyte by adding one layer of water molecules onto the catalyst surface to simulate the solvent environment.

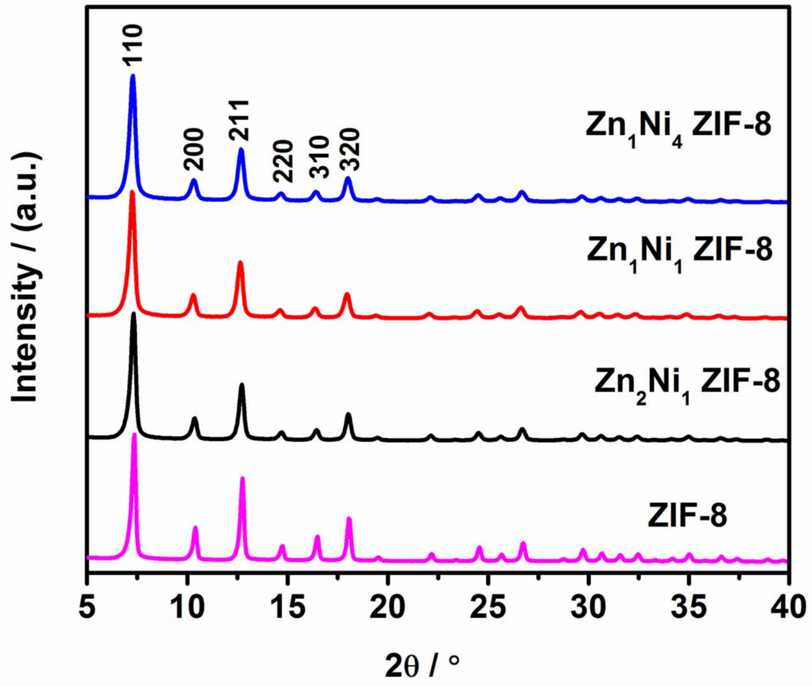

Fig. S1. XRD patterns of Zn_xNi_y ZIF-8 precursors with different Ni loadings.

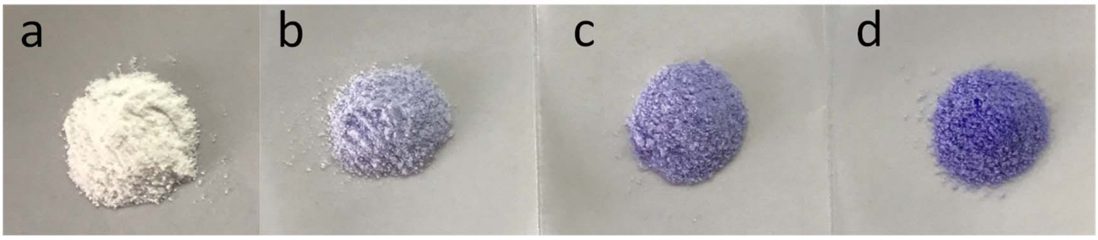

Fig. S2. Photographs of (a) ZIF-8, (b) Zn_2Ni_1 ZIF-8, (c) Zn_1Ni_1 ZIF-8 and (d) Zn_1Ni_4 ZIF-8.

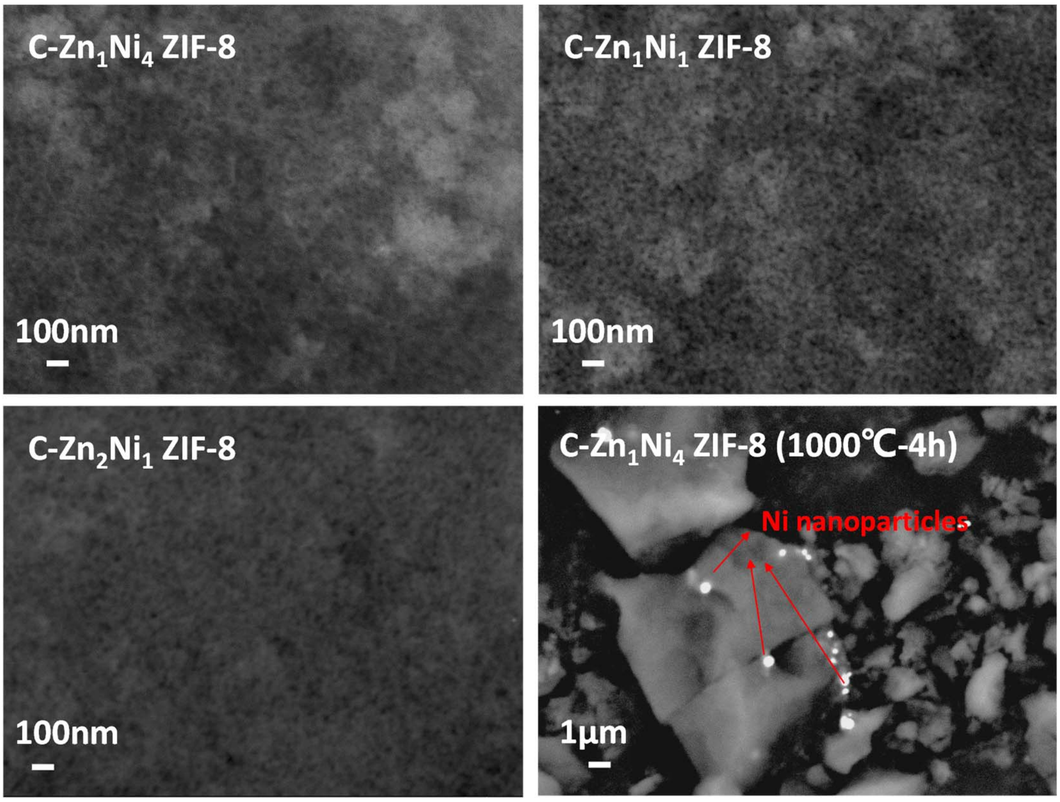

Fig. S3. Backscattered SEM images of the pyrolysis products, C-Zn$_2$Ni$_1$ ZIF-8, C-Zn$_1$Ni$_1$ ZIF-8, C-Zn$_1$Ni$_4$ ZIF-8 and C-Zn$_1$Ni$_4$ ZIF-8 (1000 ºC-4h).

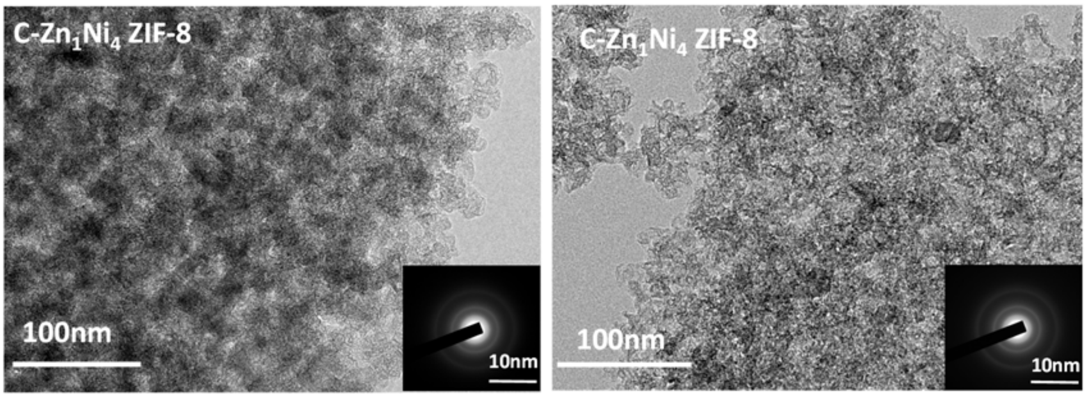

Fig. S4. HRTEM images of C-Zn$_1$Ni$_4$ ZIF-8 in different regions and the corresponding SAED patterns.

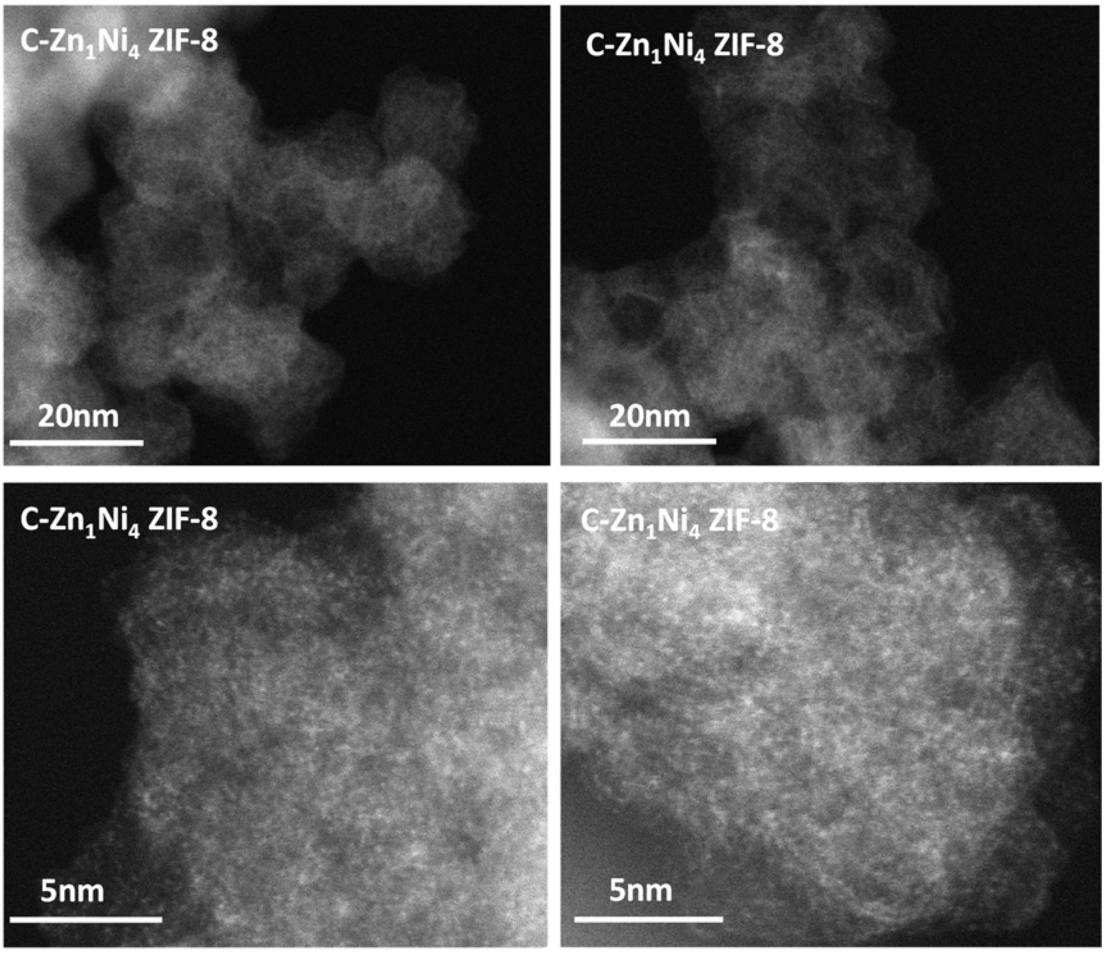

Fig. S5. HAADF-STEM images of C-Zn_1Ni_4 ZIF-8 in different regions.

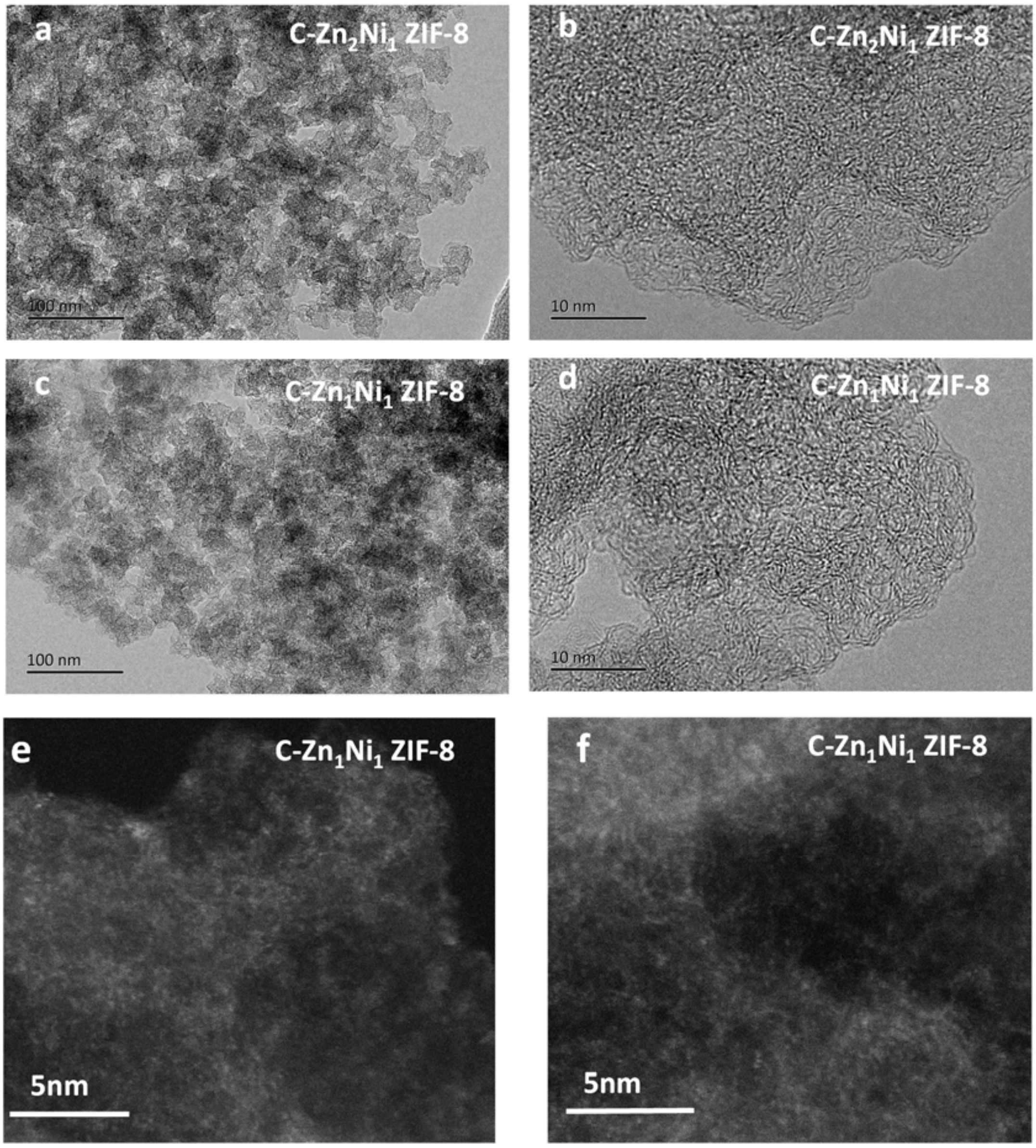

Fig. S6. TEM and HRTEM images of (a,b) C-Zn$_2$Ni$_1$ ZIF-8; (c,d) C-Zn$_1$Ni$_1$ ZIF-8 and (e-f) HAADF-STEM images of C-Zn$_1$Ni$_1$ ZIF-8.

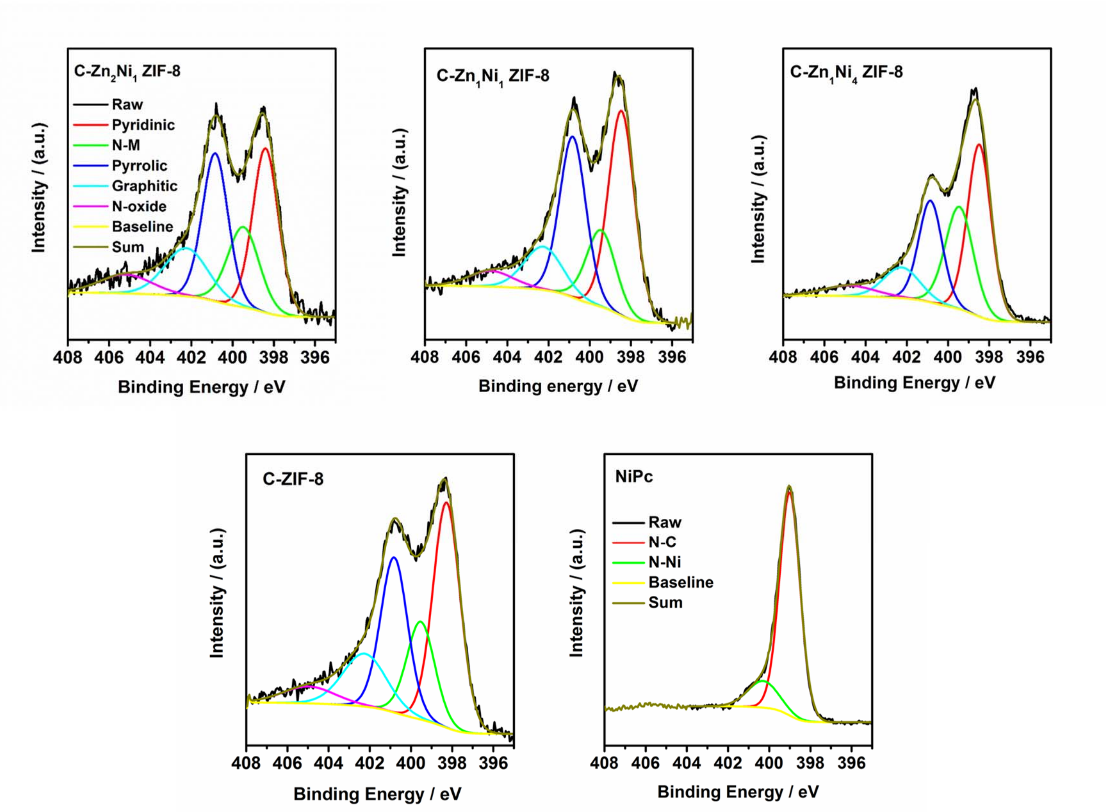

Fig. S7. N1s XPS spectra of C-Zn$_x$Ni$_y$ ZIF-8 and NiPc. *N-M stands for N-metal.

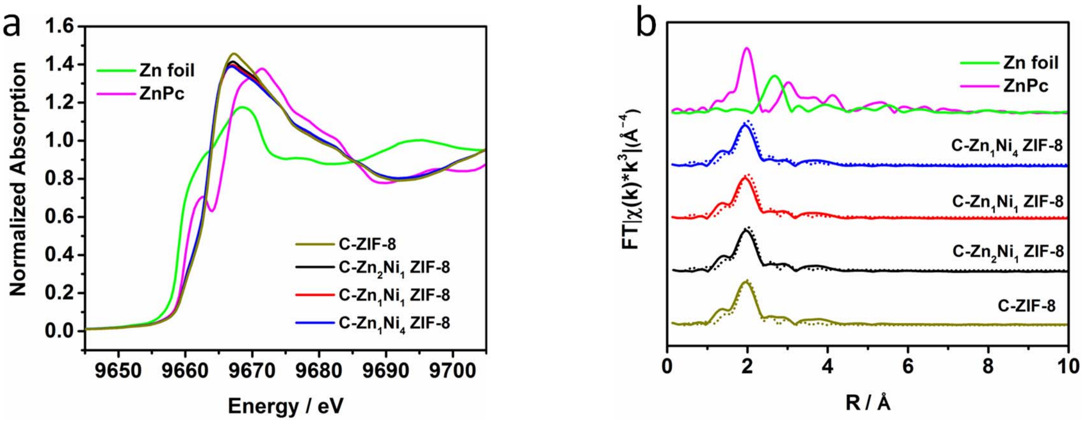

Fig. S8 (a) XANES spectra and (b) Fourier transformed EXAFS spectra of Zn K-edge for C-Zn$_x$Ni$_y$ ZIF-8 and the corresponding reference samples (solid lines stand for as obtained data and dotted lines denote for fitting curves).

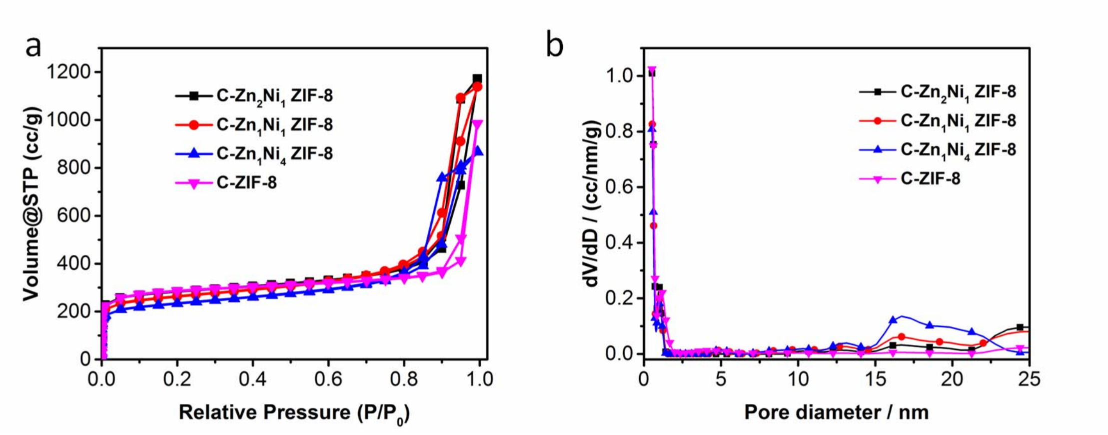

Fig. S9. (a) Nitrogen adsorption–desorption isotherms, (b) Pore size distribution of C-Zn_xNi_y ZIF-8.

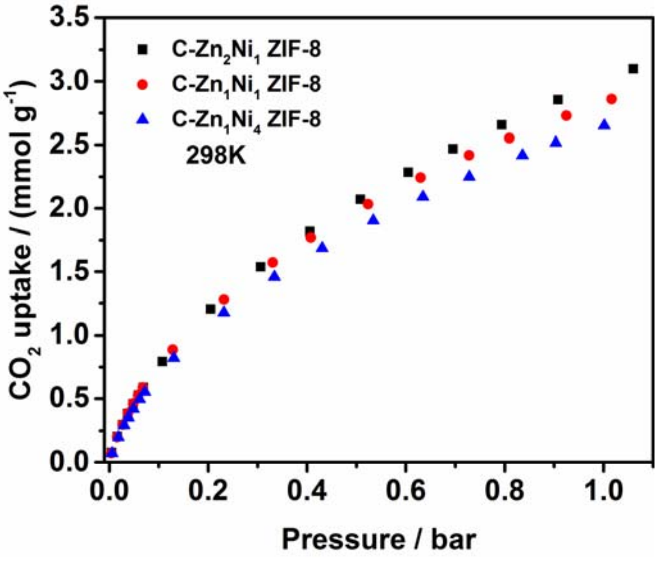

Fig. S10. CO_2 adsorption isotherms of C-Zn_2Ni_1 ZIF-8, C-Zn_1Ni_1 ZIF-8 and C-Zn_1Ni_4 ZIF-8 collected at 298 K.

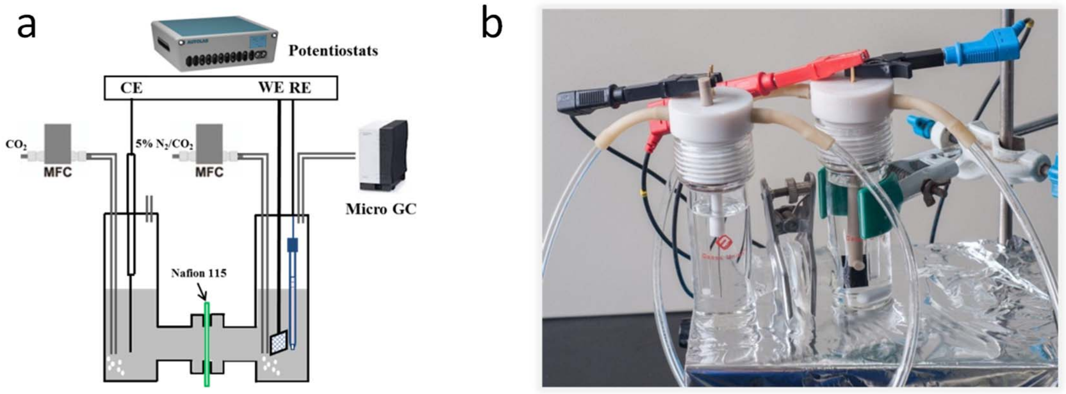

Fig. S11. (a) Schematic illustration and (b) image of the H-cell.

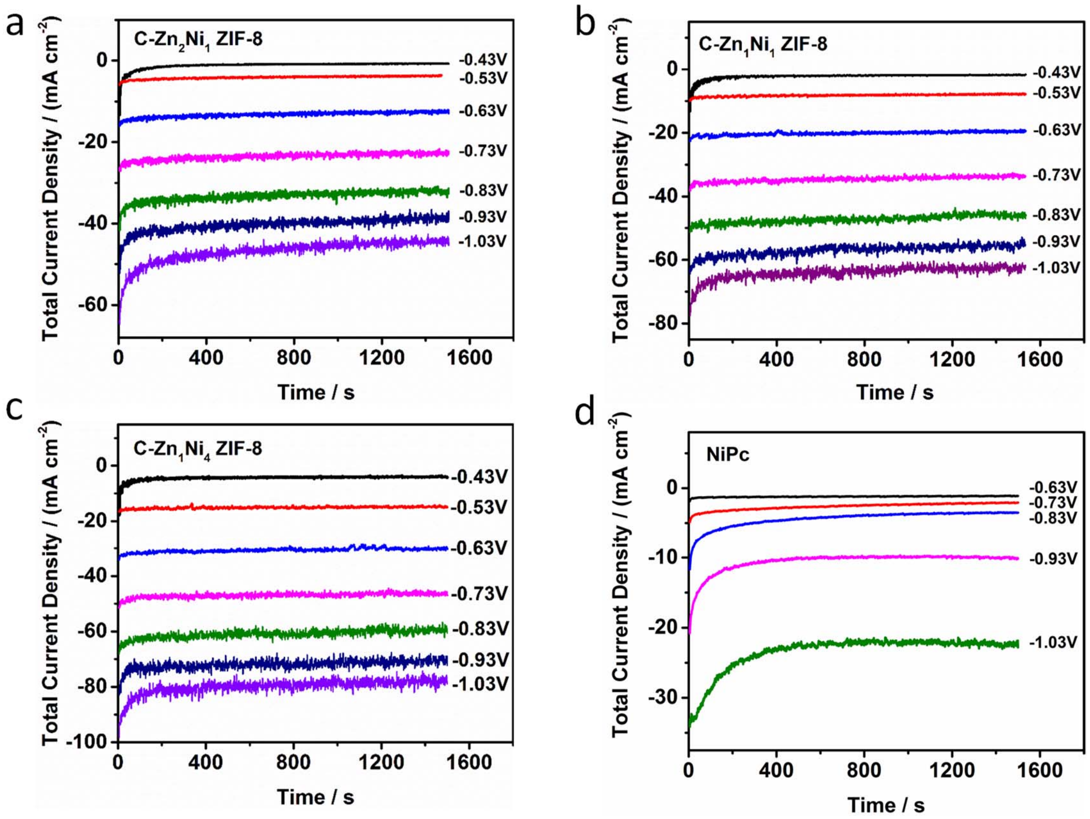

Fig. S12. Applied potential dependence of total current density over (a) C-Zn$_2$Ni$_1$ ZIF-8,(b) C-Zn$_1$Ni$_1$ ZIF-8, (c) C-Zn$_1$Ni$_4$ ZIF-8 and (d) NiPc electrode in CO$_2$-saturated 1M KHCO$_3$ solution with a catalyst loading of 2.0±0.1 mg cm^{-2} for C-Zn$_x$Ni$_y$ ZIF-8 and 1.06 mg cm^{-2} for NiPc.

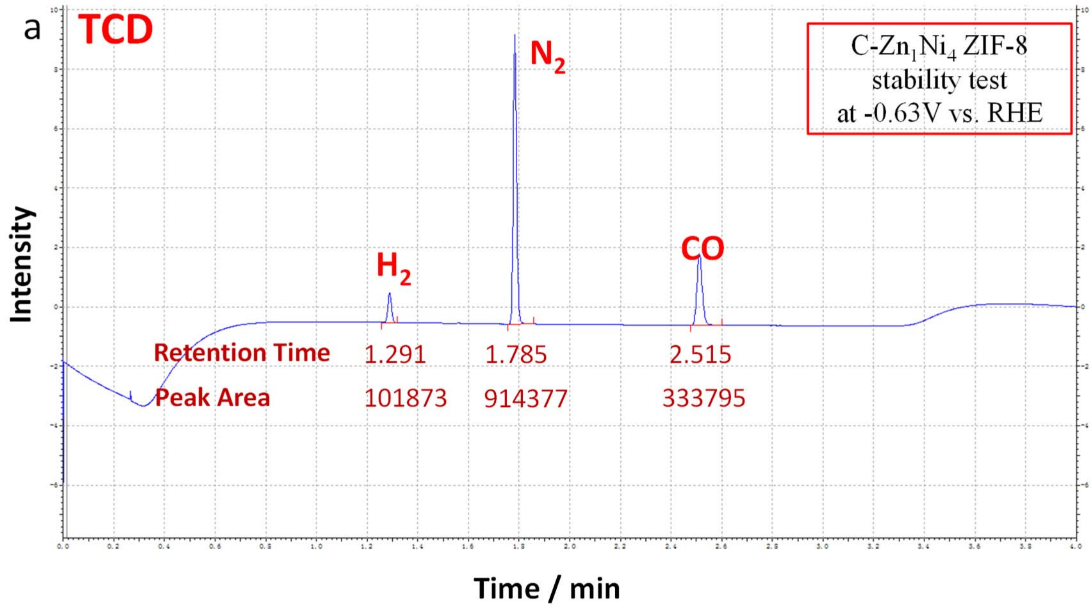

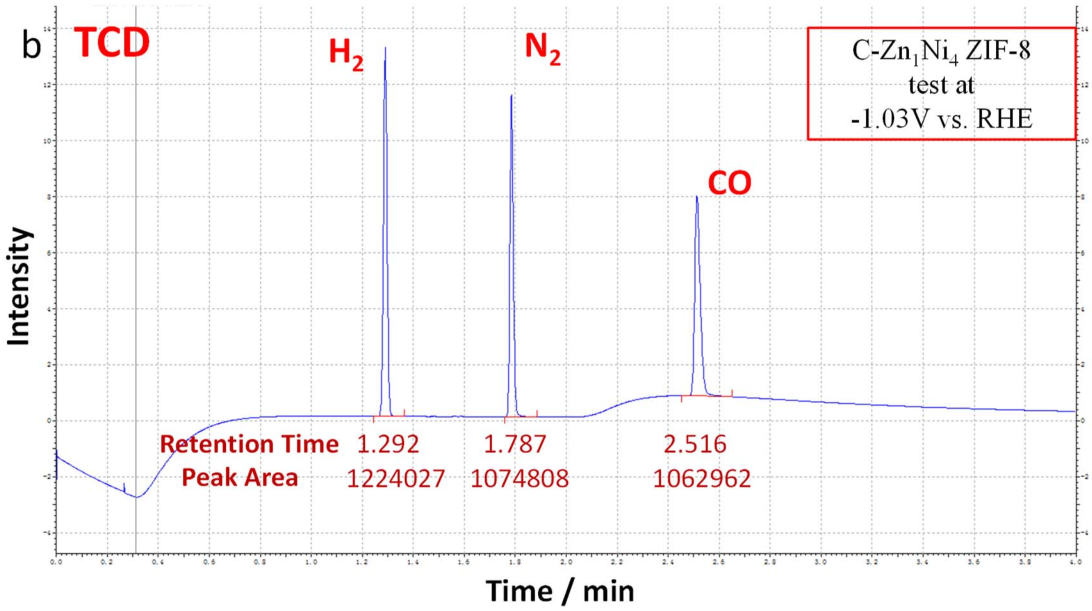

Fig. S13. Products detection. GC plots of the gas products.

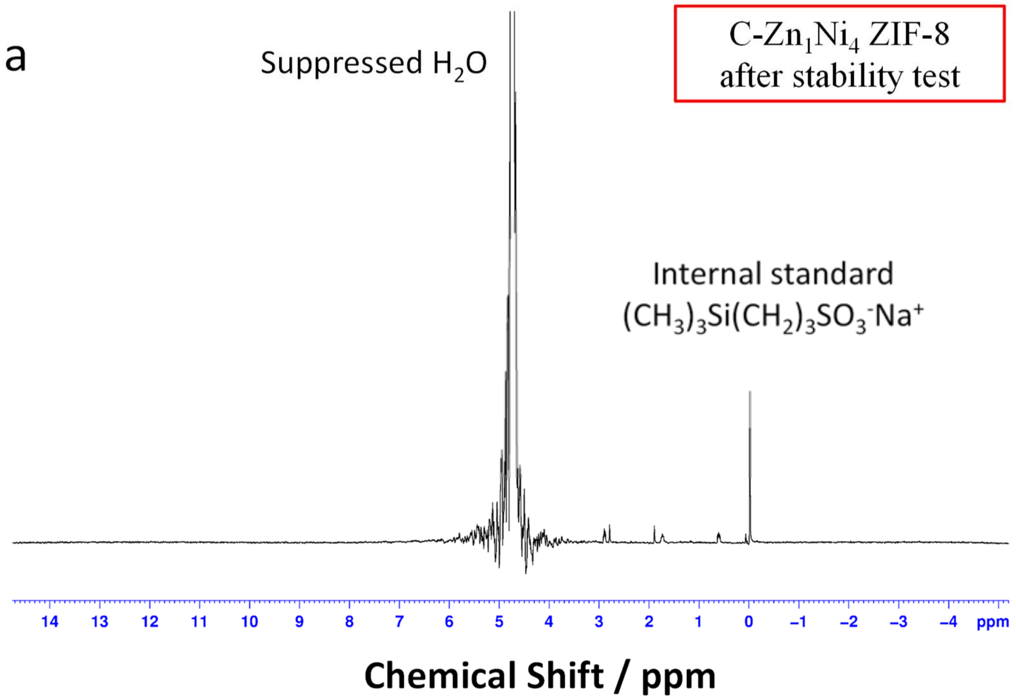

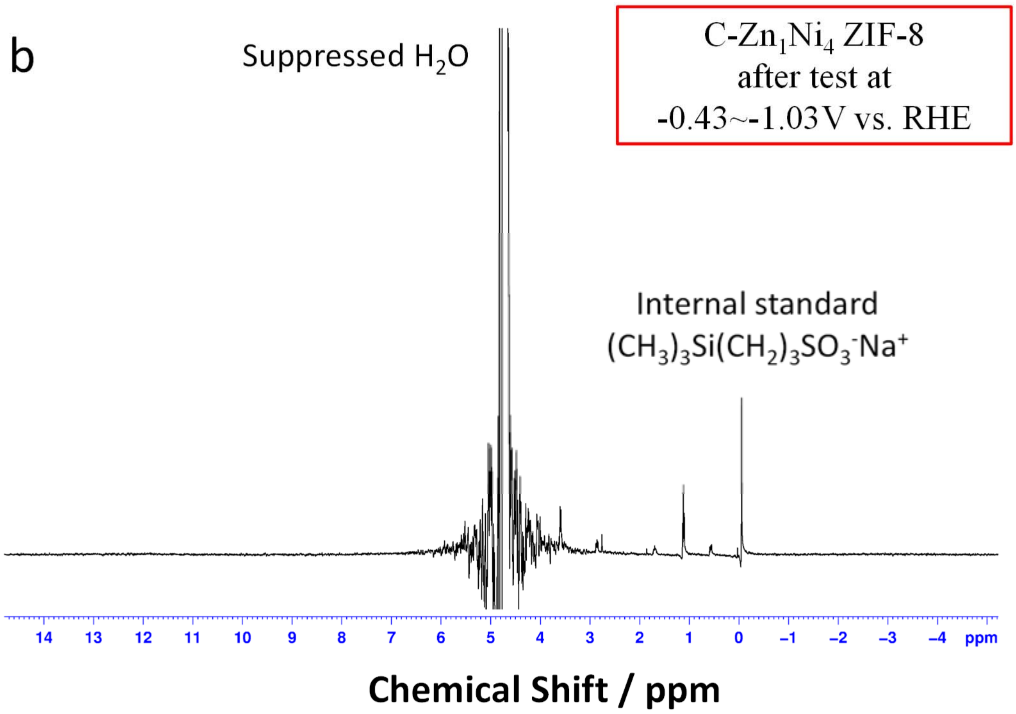

Fig. S14. Products detection. NMR spectra of the liquid products.

*The chemical shift for $HCOO^-$ is around 8.47.

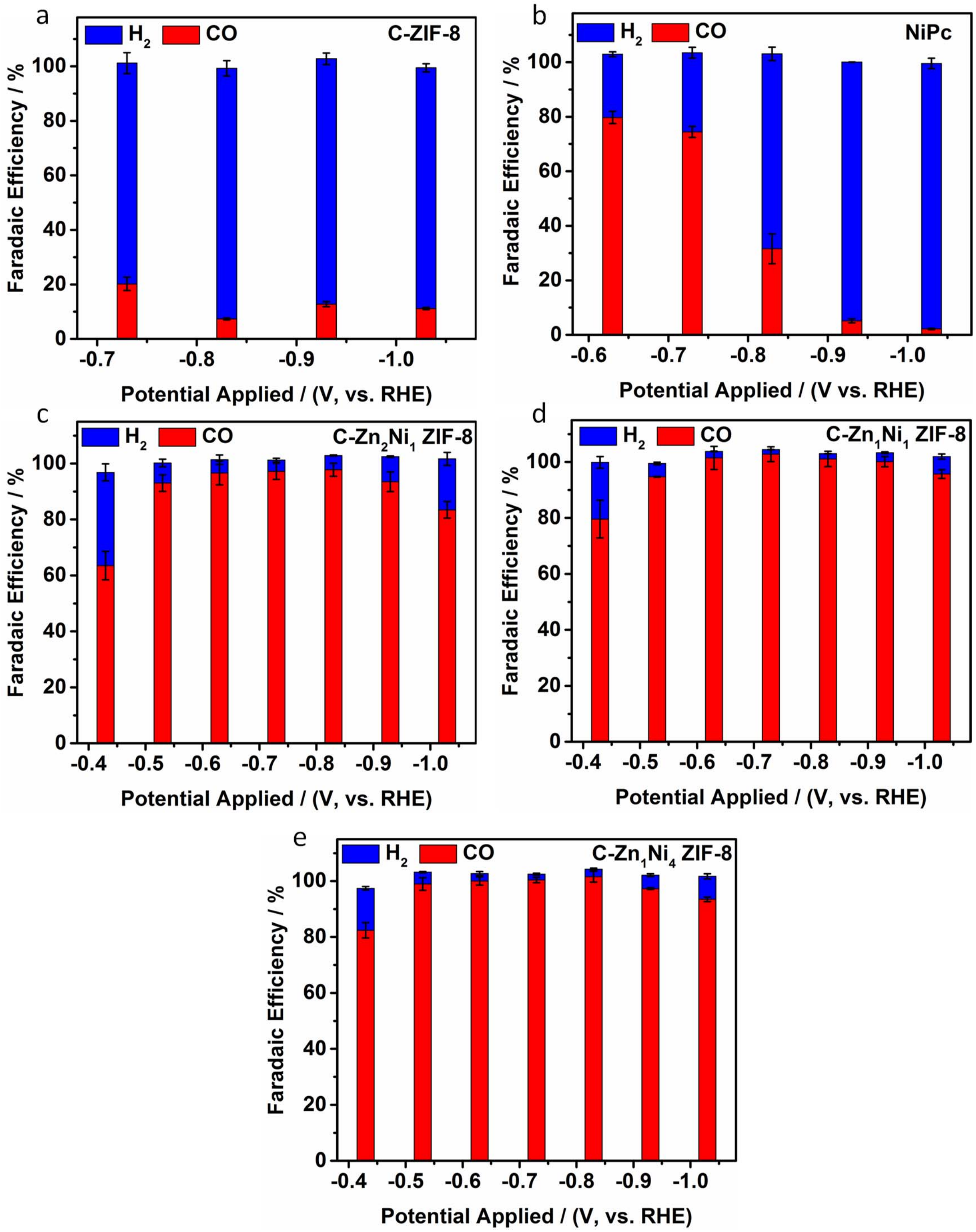
a
H$_2$
CO
C-ZIF-8
Faradaic Efficiency / %
0
20
40
60
80
100
-0.7
-0.8
-0.9
-1.0
Potential Applied / (V, vs. RHE)
b
H$_2$
CO
NiPc
Faradaic Efficiency / %
0
20
40
60
80
100
-0.6
-0.7
-0.8
-0.9
-1.0
Potential Applied / (V vs. RHE)
c
H$_2$
CO
C-Zn$_2$Ni$_1$ ZIF-8
Faradaic Efficiency / %
0
20
40
60
80
100
-0.4
-0.5
-0.6
-0.7
-0.8
-0.9
-1.0
Potential Applied / (V, vs. RHE)
d
H$_2$
CO
C-Zn$_1$Ni$_1$ ZIF-8
Faradaic Efficiency / %
0
20
40
60
80
100
-0.4
-0.5
-0.6
-0.7
-0.8
-0.9
-1.0
Potential Applied / (V, vs. RHE)
e
H$_2$
CO
C-Zn$_1$Ni$_4$ ZIF-8
Faradaic Efficiency / %
0
20
40
60
80
100
-0.4
-0.5
-0.6
-0.7
-0.8
-0.9
-1.0
Potential Applied / (V, vs. RHE)

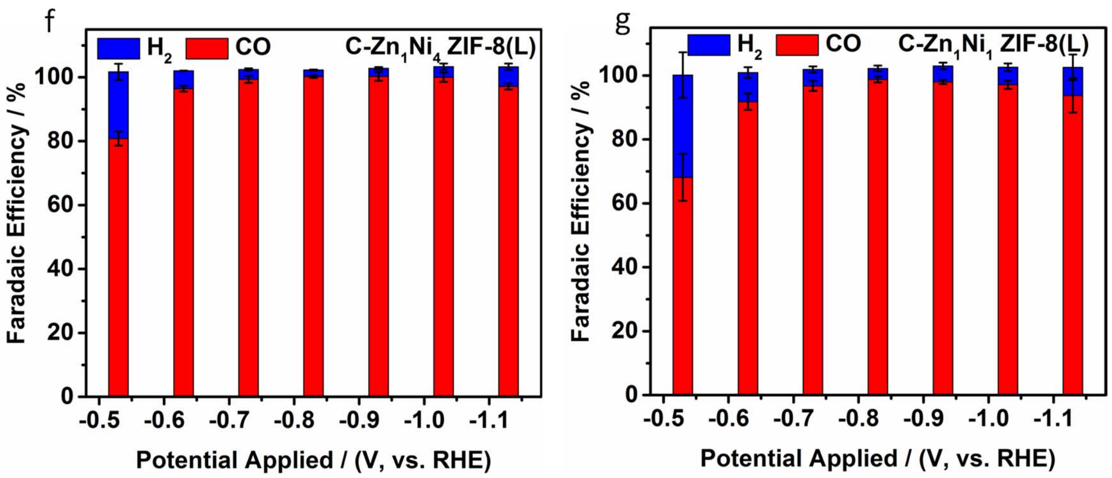

Fig. S15. Applied potential dependence of CO and H_2 Faradaic efficiencies before normalization process on (a) C-ZIF-8, (b) NiPc, (c) C-Zn_2Ni_1 ZIF-8, (d) C-Zn_1Ni_1 ZIF-8 and (e) C-Zn_1Ni_4 ZIF-8 electrode in CO_2-saturated 1 M $KHCO_3$ solution with a catalyst loading of 2.0 ± 0.1 mg cm^{-2} for C-Zn_xNi_y ZIF-8 and 1.06 mg cm^{-2} for NiPc . (f) C-Zn_1Ni_4 ZIF-8 and (g) C-Zn_1Ni_1 ZIF-8 electrode in CO_2-saturated 0.5 M $KHCO_3$ solution with a catalyst loading of 0.088 mg cm^{-2} for C-Zn_1Ni_4 ZIF-8 and 0.226 mg cm^{-2} for C-Zn_1Ni_1 ZIF-8.

*L stands for low loading in the TOF determination part.

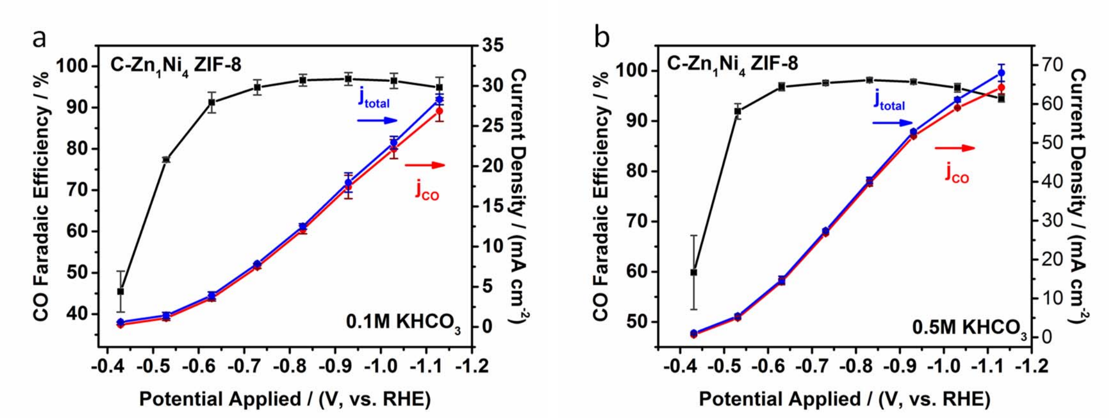

Fig. S16. CO_2 electroreduction performances of C-Zn_1Ni_4 ZIF-8 electrode in (a) CO_2-saturated 0.1 M $KHCO_3$ solution and (b) CO_2-saturated 0.5 M $KHCO_3$ solution with a catalyst loading of 2.0 ± 0.1 mg cm^{-2}.

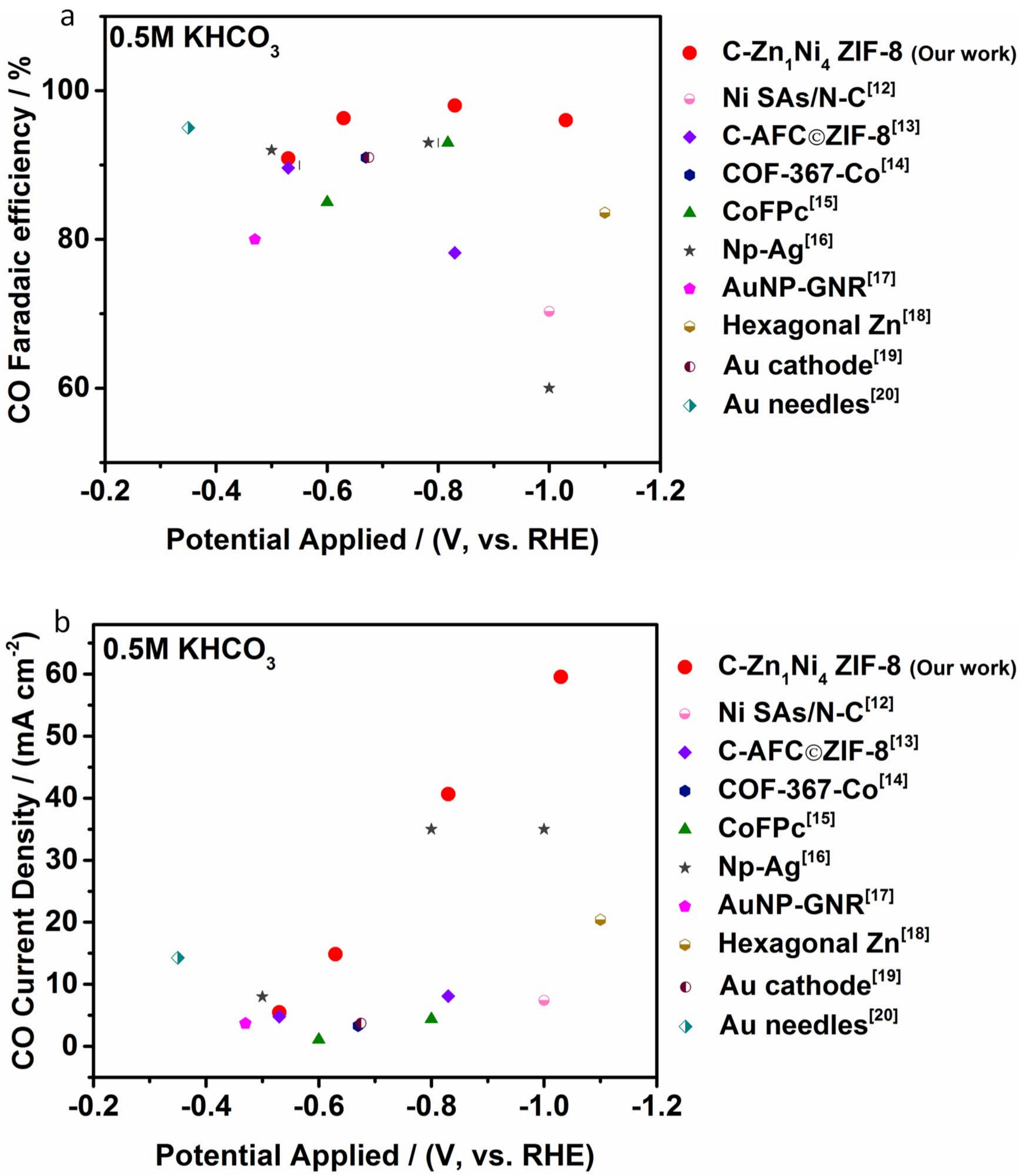
a
0.5M KHCO3
CO Faradaic efficiency / %
100
80
60
-0.2
-0.4
-0.6
-0.8
-1.0
-1.2
Potential Applied / (V, vs. RHE)
C-Zn1Ni4 ZIF-8 (Our work)
Ni SAs/N-C[12]
C-AFC©ZIF-8[13]
COF-367-Co[14]
CoFPc[15]
Np-Ag[16]
AuNP-GNR[17]
Hexagonal Zn[18]
Au cathode[19]
Au needles[20]
b
0.5M KHCO3
CO Current Density / (mA cm-2)
60
50
40
30
20
10
0
-0.2
-0.4
-0.6
-0.8
-1.0
-1.2
Potential Applied / (V, vs. RHE)
C-Zn1Ni4 ZIF-8 (Our work)
Ni SAs/N-C[12]
C-AFC©ZIF-8[13]
COF-367-Co[14]
CoFPc[15]
Np-Ag[16]
AuNP-GNR[17]
Hexagonal Zn[18]
Au cathode[19]
Au needles[20]

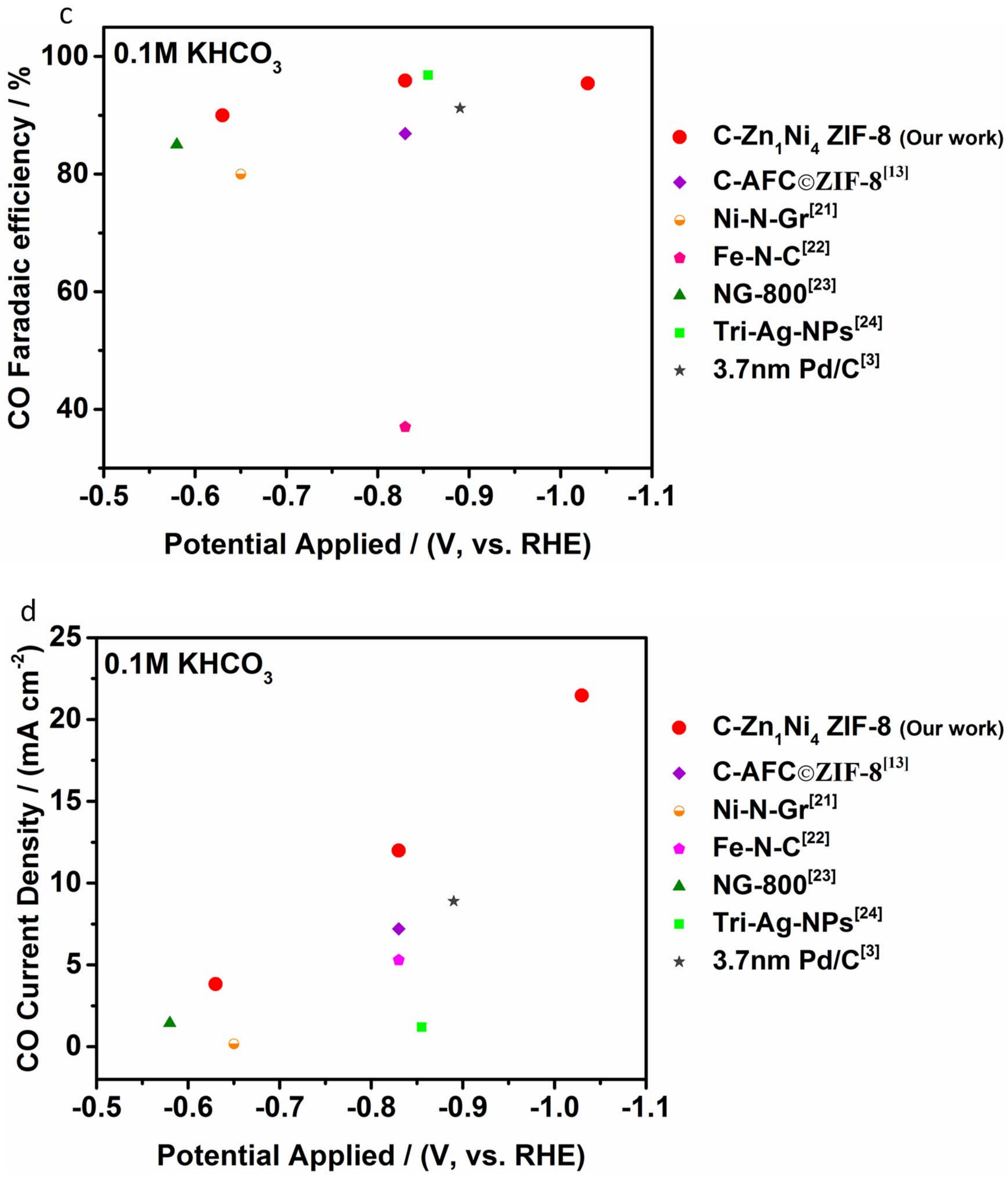

Fig. S17. Comparison of various catalysts for CO_2 electroreduction to CO in CO_2-saturated 0.5 M $KHCO_3$ and 0.1 M $KHCO_3$ solution with a catalyst loading of 2 mg cm^{-2} for C-Zn_1Ni_4 ZIF-8 . (a, c) CO Faradaic efficiency and (b, d) CO partial current density normalized to geometric area.

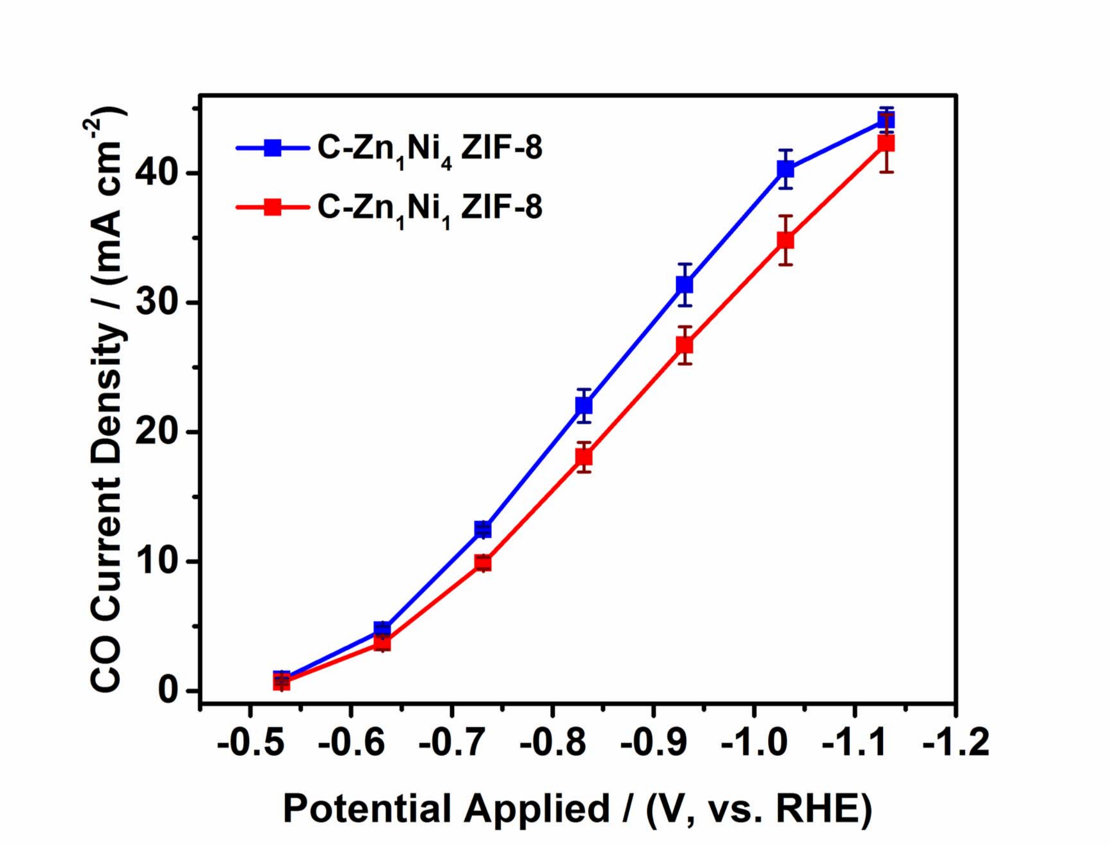

Fig. S18. Applied potential dependence of CO partial current density in CO_2-saturated 0.5 M $KHCO_3$ solution with a catalyst loading of 0.088 mg cm^{-2} for C-Zn_1Ni_4 ZIF-8 and 0.226 mg cm^{-2} for C-Zn_1Ni_1 ZIF-8.

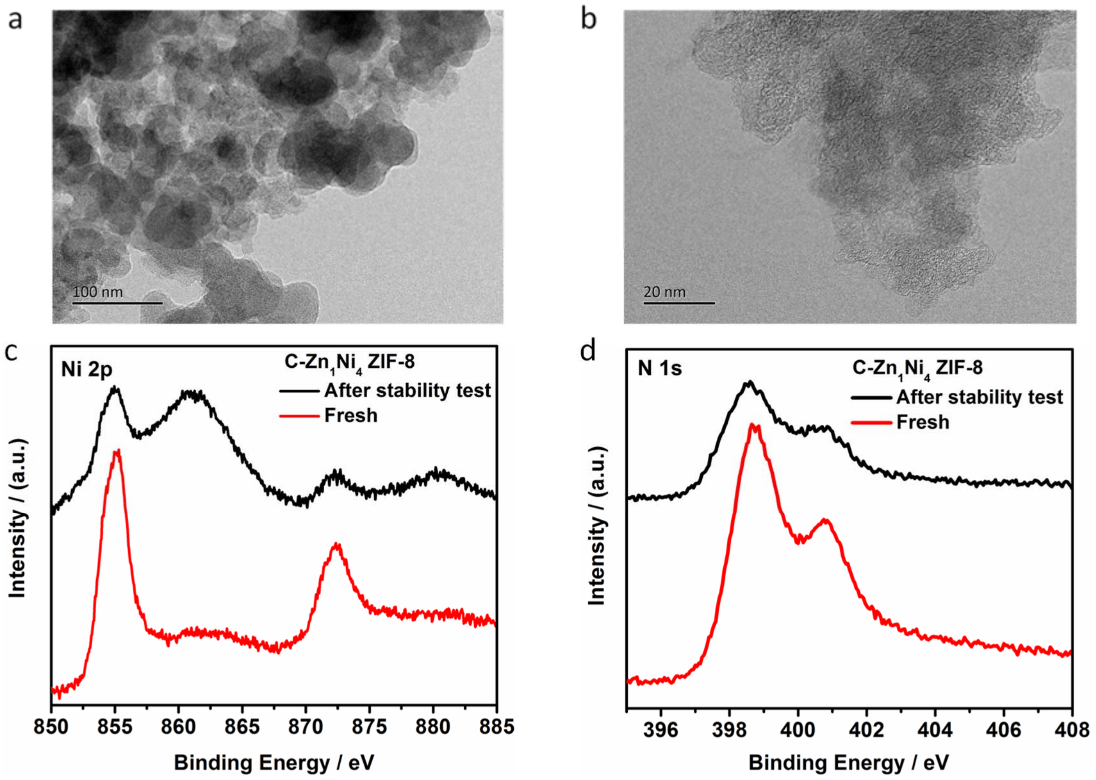

Fig. S19. (a) TEM and (b) HRTEM images and XPS spectra of (c) Ni 2p, (d) N1s for C-Zn$_1$Ni$_4$ ZIF-8 collected from the porous electrode after 720 min stability test.

*In the TEM images, these spherical nanoparticles are Vulcan XC-72R on the diffusion layer.

* In the Ni XPS spectra, the increased intensity around 861eV and 880 eV arise from F KL2 and F KL3 respectively. The F element originates from Nafion ionomer which was introduced when preparing the catalyst layer.

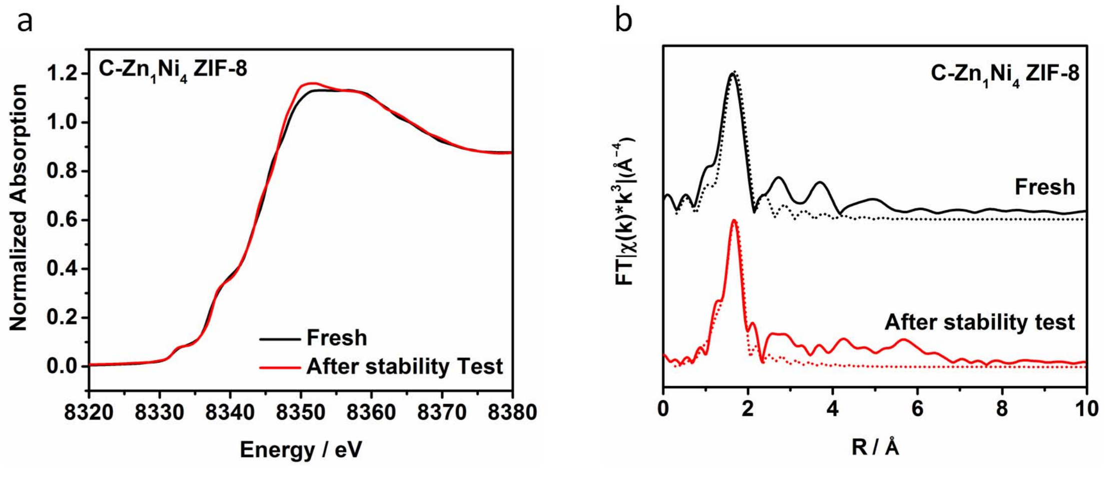

Fig. S20. (a) XANES spectra and (b) Fourier transformed EXAFS spectra of Ni K-edge for C-Zn$_1$Ni$_4$ ZIF-8 before and after 720 min stability test.

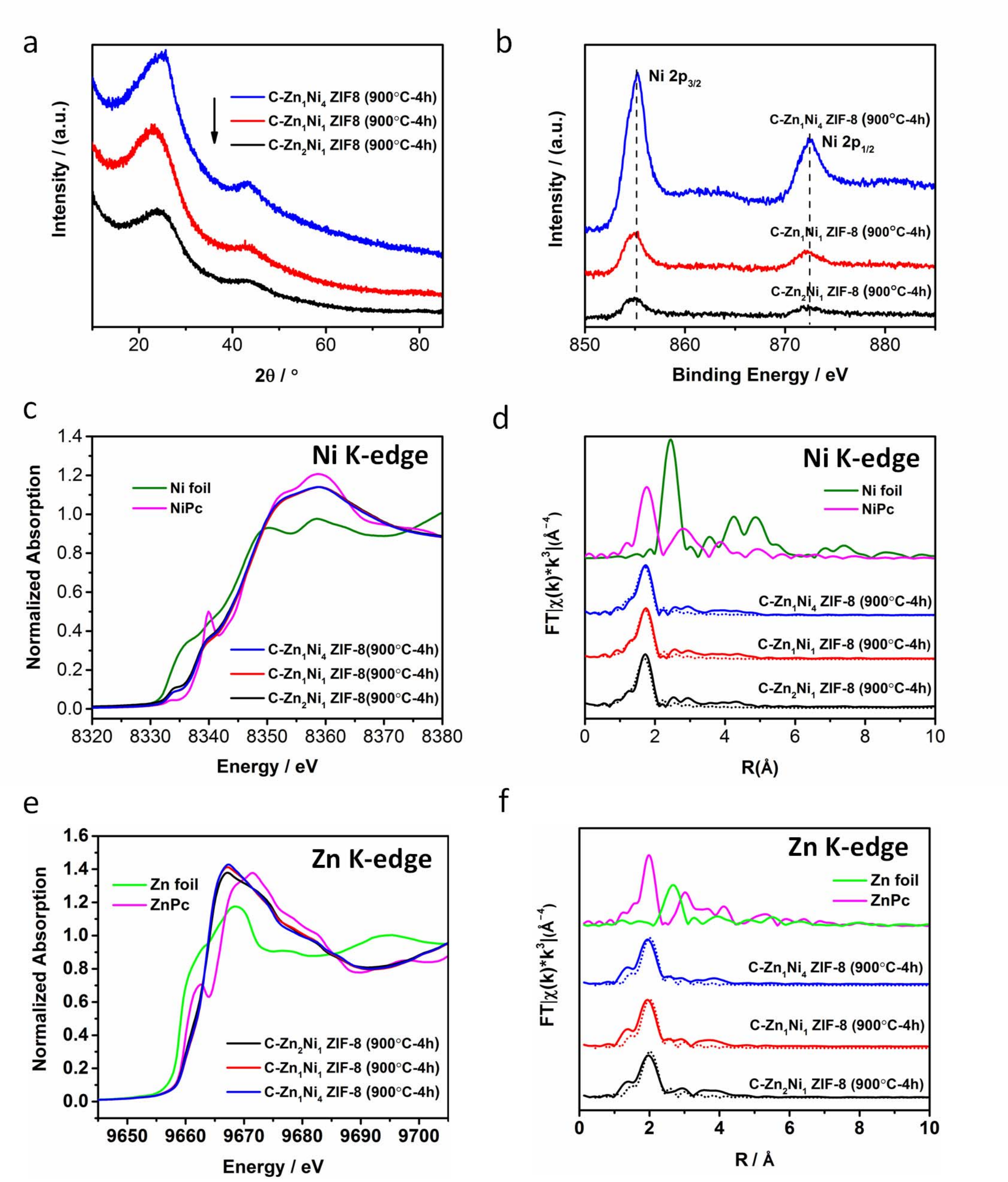

Fig. S21. Characterizations of C-Zn_xNi_y ZIF-8 (900ºC-4h). (a) XRD patterns, (b) Ni 2p high-resolution XPS surveys of C-Zn_xNi_y ZIF-8 (900ºC-4h). (c-d) XANES spectra and Fourier transformed EXAFS spectra of Ni K-edge, (e-f) XANES spectra and Fourier transformed EXAFS spectra of Zn K-edge of C-Zn_xNi_y ZIF-8 (900ºC-4h) and the corresponding reference samples.

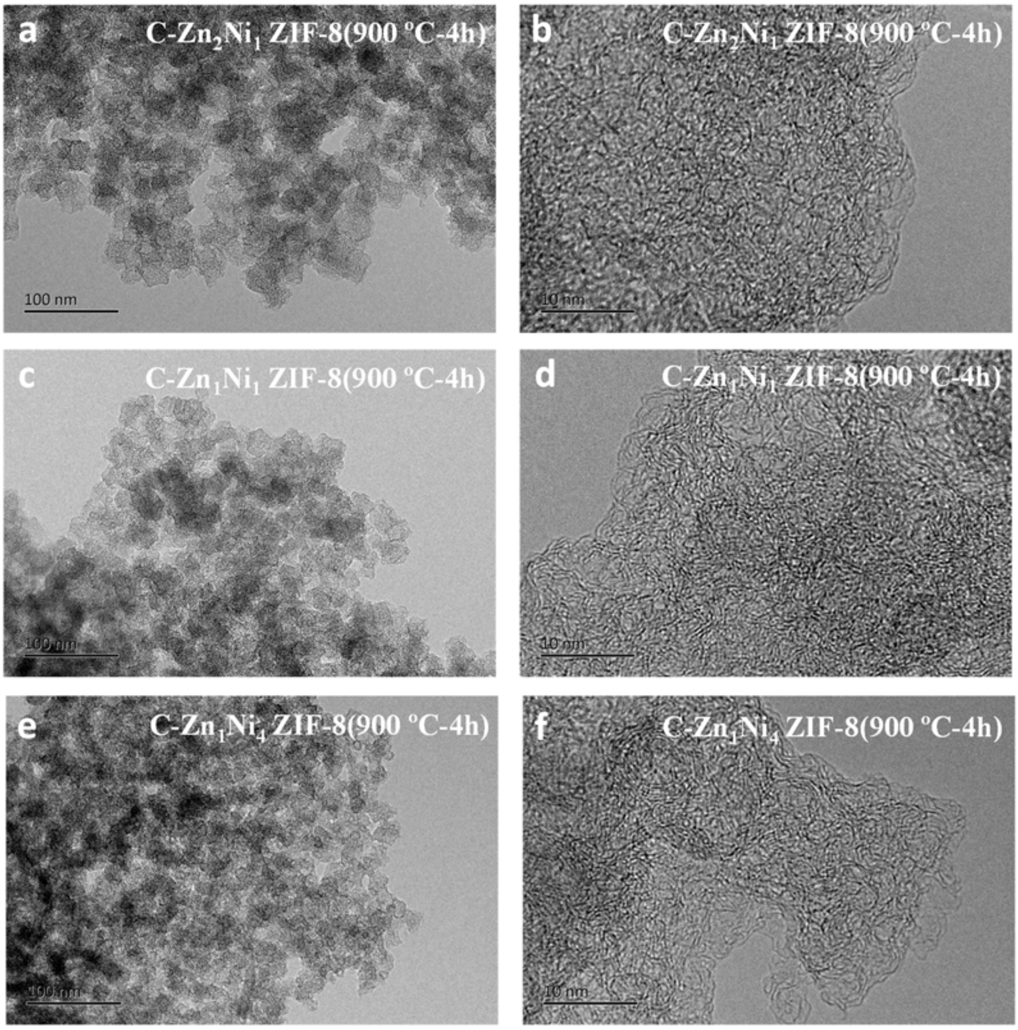

Fig. S22. TEM and HRTEM images of C-Zn$_x$Ni$_y$ ZIF-8 (900ºC-4h).

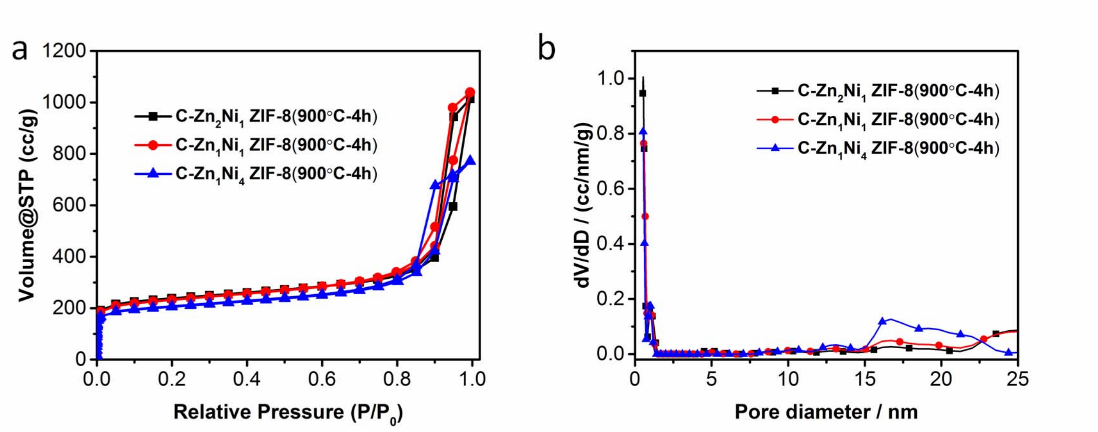

Fig. S23. (a) Nitrogen adsorption–desorption isotherms, (b) Pore size distributions of C-Zn$_x$Ni$_y$ ZIF-8 (900ºC-4h).

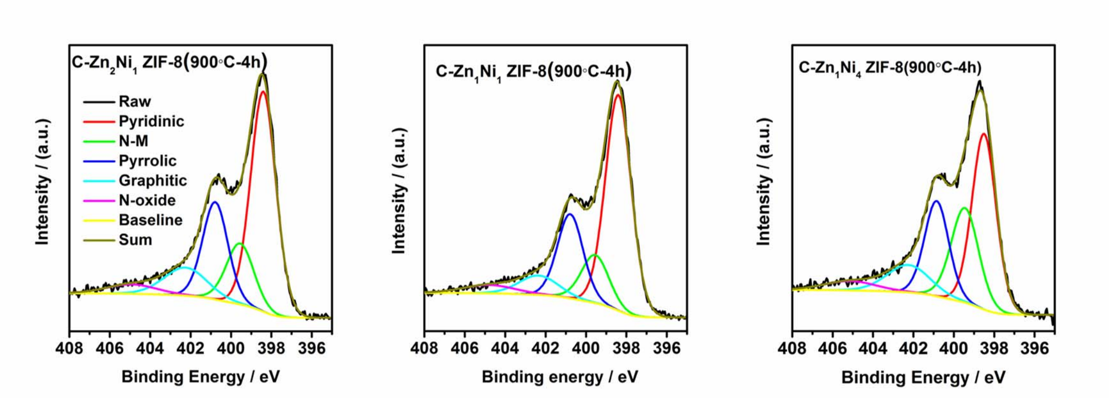

Fig. S24. N1s XPS spectra of C-Zn$_x$Ni$_y$ ZIF-8 (900ºC-4h).

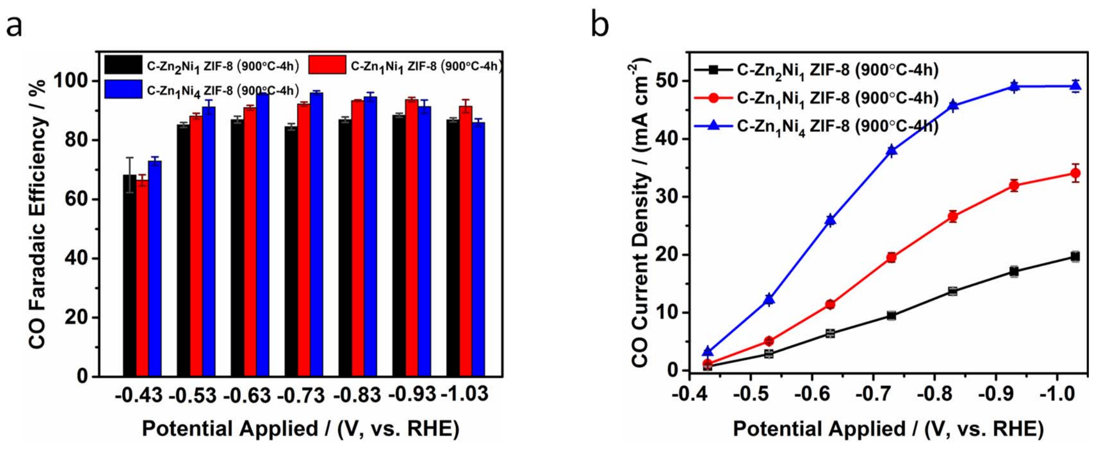

Fig. S25. (a) Applied potential dependence of CO Faradaic efficiency, (b) CO partial current density over C-Zn$_x$Ni$_y$ ZIF-8 (900ºC-4h) in CO$_2$-saturated 1 M KHCO$_3$ solution.

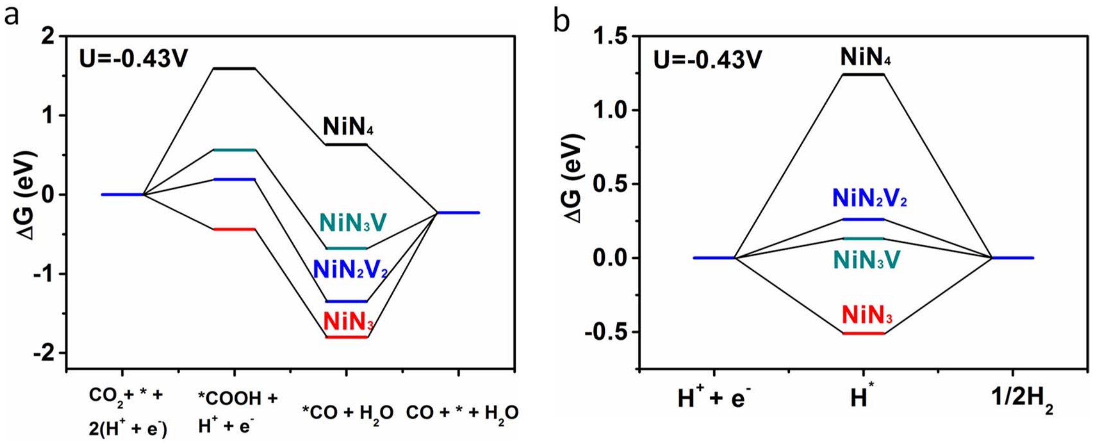

Fig. S26. Free energy diagrams with solvation effect corrections for (a) CO$_2$RR and (b) HER at U=−0.43 V.

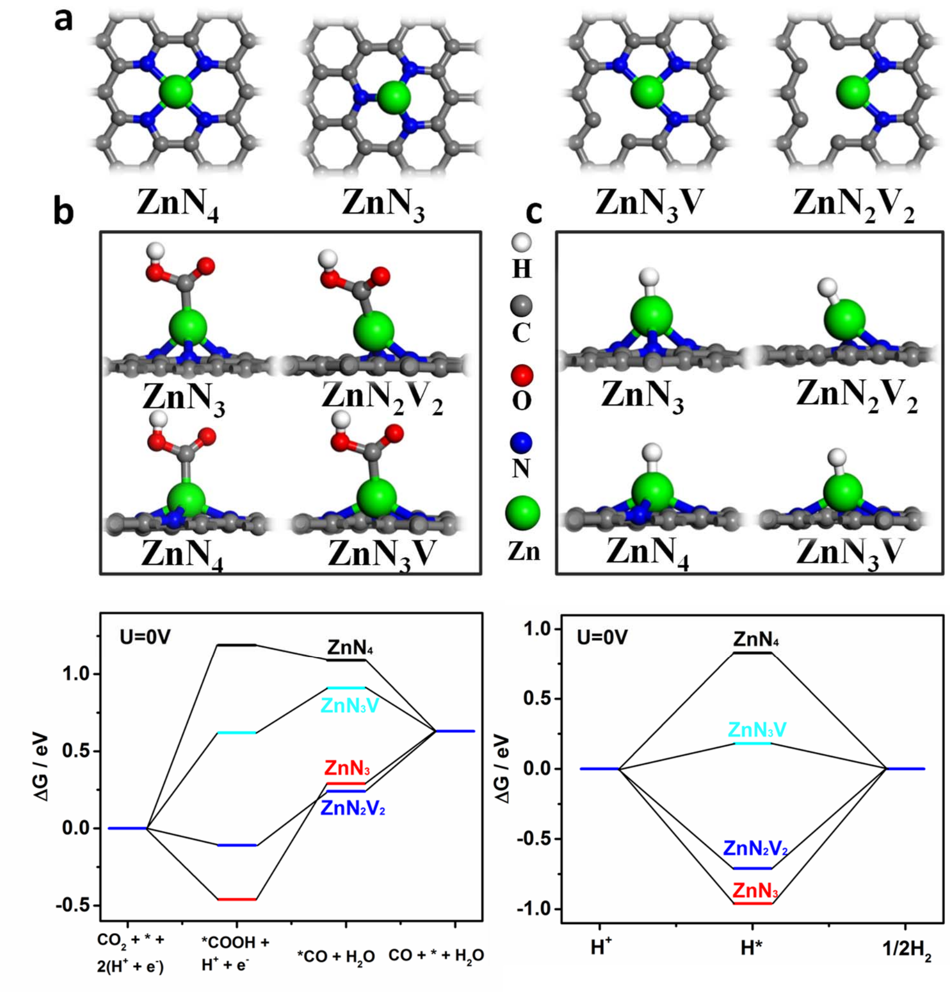

Fig. S27. DFT calculations for Zn-N$_x$ sites. (a) Optimized atomic structures of different Zn-N structures with Zn atoms coordinated with 4 N atoms (ZnN_4), 3 N atoms (ZnN_3 and ZnN_3V), 2 N atoms (ZnN_2V_2), (b-c) Free energy diagrams with solvation effect corrections for CO_2RR (b) and HER (c) pathways on Zn sites of different Zn-N structures at 0 V. Optimized atomic structures for *COOH and *H intermediates adsorbed on Zn sites are shown on the top. The white, grey, red, blue, green balls represent H, C, O, N, Zn atoms, respectively.

* For Zn-N sites (ZnN_4, ZnN_3, ZnN_3V, ZnN_2V_2), G_{*COOH} (1.19 eV, -0.46 eV, 0.62 eV, -0.11 eV, respectively) are all significantly higher than G_{*H} (0.83 eV, -0.96 eV, 0.18 eV, -0.71 eV, respectively), revealing that they all have low CO_2RR selectivity. Moreover, for ZnN_3, ZnN_3V and ZnN_2V, G_{*CO} are much higher than G_{*COOH}, indicating that the formation of CO is relatively difficult. Therefore, on these Zn-N sites the reaction is predominately HER with very little CO generation. Such result corresponds well with the poor CO_2RR activity on C-ZIF-8.

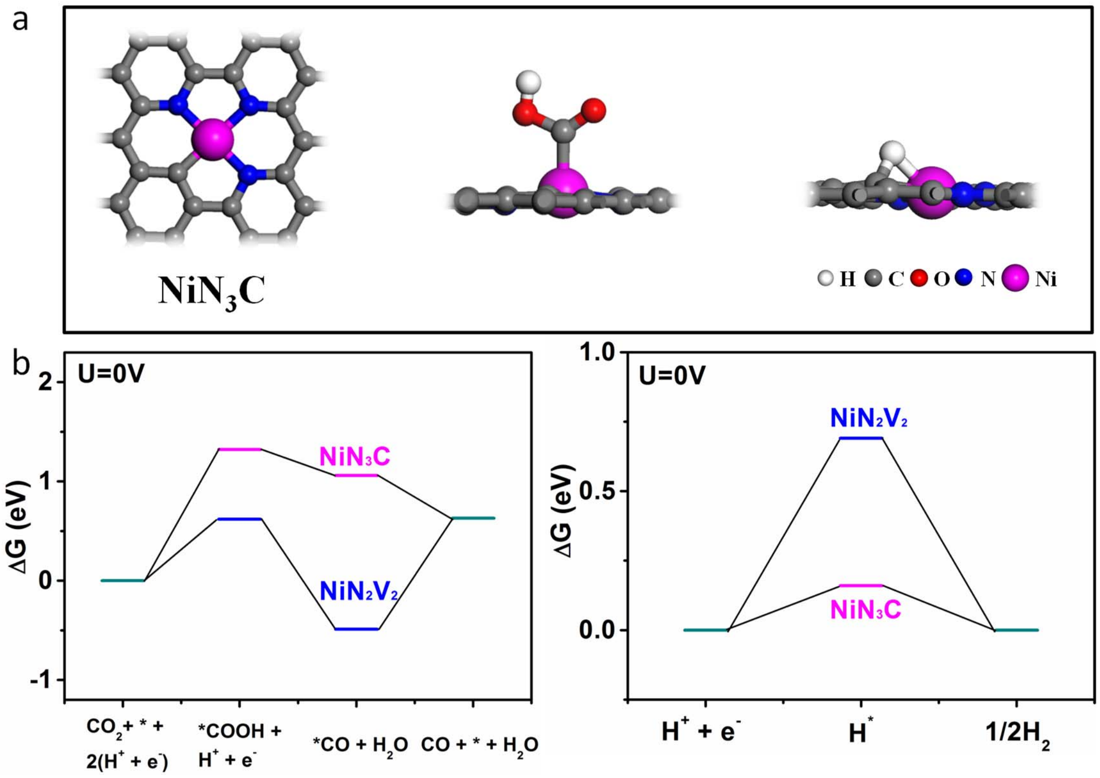

Fig. S28. DFT calculations of supplemental structure of NiN_3C. (a) Optimized atomic structures of NiN_3C and NiN_3C with *COOH and *H intermediates adsorbed on Ni site. (b) Free energy diagrams with solvation effect corrections for CO_2RR (left) and HER (right) at U=0 V.

Table S1. Ni content (wt%) of Zn_xNi_y ZIF-8 precursors as measured by ICP-OES.

Sample	**Zn_2Ni_1 ZIF-8**	**Zn_1Ni_1 ZIF-8**	**Zn_1Ni_4 ZIF-8**
Ni wt%	0.25	0.54	1.79

Table S2. Ni and Zn contents (wt%) of C-Zn_xNi_y ZIF-8 as measured by ICP-OES and derived from XPS analysis.

Sample	**C-Zn_2Ni_1 ZIF-8**	**C-Zn_1Ni_1 ZIF-8**	**C-Zn_1Ni_4 ZIF-8**
Ni wt%-ICP	0.93	2.07	5.44
Zn wt%-ICP	3.22	2.91	3.29
Ni wt%-XPS	0.94	2.06	5.49
Zn wt%-XPS	2.88	2.81	3.08

*C-ZIF-8, Zn wt% = 4.38% (ICP-OES).

Table S3. The total nitrogen content and percentage of different nitrogen species in C-Zn_xNi_y ZIF-8.

Sample	**C-Zn_2Ni_1 ZIF-8**	**C-Zn_1Ni_1 ZIF-8**	**C-Zn_1Ni_4 ZIF-8**	**C-ZIF-8**
N wt%	6.36	7.29	10.35	6.84
Pyridinic	1.97	2.76	3.92	2.58
Metal-N(M-N)	1.18	1.15	1.64	1.15
Pyrrolic	1.78	2.17	3.08	1.77
Graphitic	0.97	0.85	1.20	0.97
N-oxide	0.46	0.36	0.51	0.37

Table S4. EXAFS data fitting results of C-Zn$_x$Ni$_y$ ZIF-8 for Ni K edge.

Sample	Ni-N CN	R (Å)	σ^2*10^2 (Å^2)	ΔE_0 (eV)	R factor
C-Zn$_2$Ni$_1$ ZIF-8	2.6 ± 0.4	1.86 ± 0.01			
C-Zn$_1$Ni$_1$ ZIF-8	2.7 ± 0.4	1.87 ± 0.01	0.3 ± 0.1	-5.3 ± 0.9	0.1003
C-Zn$_1$Ni$_4$ ZIF-8	2.4 ± 0.4	1.88 ± 0.01			

Table S5. EXAFS data fitting results of C-Zn$_x$Ni$_y$ ZIF-8 for Zn K edge.

Sample	Zn-N CN	R (Å)	σ^2*10^2 (Å^2)	ΔE_0 (eV)	R factor
C-ZIF-8	3.6 ± 0.6	2.02 ± 0.02	± 0.1	-5.3 ± 0.9	0.022
C-Zn$_2$Ni$_1$ ZIF-8	3.5 ± 0.7	2.01 ± 0.02			
C-Zn$_1$Ni$_1$ ZIF-8	3.4 ± 0.8	2.01 ± 0.02			
C-Zn$_1$Ni$_4$ ZIF-8	3.5 ± 0.9	2.01 ± 0.02			

Table S6. Porosity characters of C-Zn$_x$Ni$_y$ ZIF-8.

Catalyst	BET surface area (m^2 g^{-1})	Micropore surface area (m^2 g^{-1})	External surface area (m^2 g^{-1})	V$_{total}$ (cc g^{-1})[a]	V$_{\mu}$ (cc g^{-1})[b]
C-Zn$_2$Ni$_1$ ZIF-8	1010.8	788.0	222.8	1.81	0.35
C-Zn$_1$Ni$_1$ ZIF-8	925.5	629.7	295.8	1.76	0.28
C-Zn$_1$Ni$_4$ ZIF-8	870.8	548.8	322.1	1.34	0.22
C-ZIF-8	1004.2	853.4	150.8	1.53	0.38

Table S7. As obtained CO and H_2 Faradaic efficiencies in comparison with the CO Faradaic efficiencies after normalization process (in reference to Fig. 3a, 3c and Fig. S15) on C-Zn_xNi_y-ZIF-8.

C-ZIF-8	**-0.73V**	**-0.83V**	**-0.93V**	**-1.03V**
Normalized CO FE%	20.0	7.4	12.5	11.2
As obtained CO FE%	20.2	7.3	12.8	11.1
As obtained H_2 FE%	81.0	91.9	90.0	88.3
As obtained ($CO+H_2$) FE%	101.2	99.2	102.8	99.4

Test condition: Measured in CO_2-saturated 1 M $KHCO_3$ solution with a catalyst loading of 2.0±0.1 mg cm^{-2}.

NiPc	**-0.63V**	**-0.73V**	**-0.83V**	**-0.93V**	**-1.03V**
Normalized CO FE%	77.4	71.9	30.6	5.2	2.2
As obtained CO FE%	79.7	74.4	31.6	5.2	2.2
As obtained H_2 FE%	23.2	29.1	71.5	94.9	97.3
As obtained ($CO+H_2$) FE%	102.9	103.5	103.1	100.1	99.5

Test condition: Measured in CO_2-saturated 1 M $KHCO_3$ solution with a catalyst loading of 1.06 mg cm^{-2}.

C-Zn_2Ni_1 ZIF-8	**-0.43V**	**-0.53V**	**-0.63V**	**-0.73V**	**-0.83V**	**-0.93V**	**-1.03V**
Normalized CO FE%	65.6	92.9	95.3	95.6	95.0	91.2	82.1
As obtained CO FE%	63.5	93.0	96.6	97.2	97.8	93.5	83.4
As obtained H_2 FE%	33.3	7.2	4.8	4.0	5.1	9.0	18.2
As obtained ($CO+H_2$) FE%	96.8	100.2	101.4	101.2	102.9	102.5	101.6

Test condition: Measured in CO_2-saturated 1 M $KHCO_3$ solution with a catalyst loading of 2.0±0.1 mg cm^{-2}.

C-Zn_1Ni_1 ZIF-8	-0.43V	-0.53V	-0.63V	-0.73V	-0.83V	-0.93V	-1.03V
Normalized CO FE%	79.6	95.2	97.8	98.4	98.2	96.9	93.9
As obtained CO FE%	79.6	94.7	101.5	102.8	101.1	100.1	95.7
As obtained H_2 FE%	20.3	4.7	2.3	1.6	1.8	3.2	6.3
As obtained (CO+H_2) FE%	99.9	99.4	103.8	104.4	102.9	103.3	102.0

Test condition: Measured in CO_2-saturated 1 M $KHCO_3$ solution with a catalyst loading of 2.0±0.1 mg cm^{-2}.

C-Zn_1Ni_4 ZIF-8	-0.43V	-0.53V	-0.63V	-0.73V	-0.83V	-0.93V	-1.03V
Normalized CO FE%	84.6	95.9	97.4	98.0	97.5	95.3	91.9
As obtained CO FE%	82.4	98.9	100.0	100.3	101.6	97.3	93.5
As obtained H_2 FE%	15.0	4.2	2.7	2.1	2.6	4.8	8.2
As obtained (CO+H_2) FE%	97.4	103.1	102.7	102.4	104.2	102.1	101.7

Test condition: Measured in CO_2-saturated 1 M $KHCO_3$ solution with a catalyst loading of 2.0±0.1 mg cm^{-2}.

C-Zn_1Ni_4 ZIF-8(L*)	**-0.53V**	**-0.63V**	**-0.73V**	**-0.83V**	**-0.93V**	**-1.03V**	**-1.13V**
Normalized CO FE%	79.5	94.5	97.0	98.0	97.5	96.8	94.0
As obtained CO FE%	80.8	96.4	99.3	100.2	100.2	100.0	97.1
As obtained H_2 FE%	20.9	5.6	3.1	2.1	2.6	3.3	6.2
As obtained ($CO+H_2$) FE%	101.7	102.0	102.4	102.3	102.8	103.3	103.3

Test condition: Measured in CO_2-saturated 0.5 M $KHCO_3$ solution with a catalyst loading of 0.088 mg cm^{-2}.

*L stands for low loading in the TOF determination part.

C-Zn_1Ni_1 ZIF-8(L)	**-0.53V**	**-0.63V**	**-0.73V**	**-0.83V**	**-0.93V**	**-1.03V**	**-1.13V**
Normalized CO FE%	68.0	91.0	95.0	96.6	95.1	94.7	91.4
As obtained CO FE%	68.1	91.8	96.8	98.7	98.0	97.1	93.8
As obtained H_2 FE%	32.0	9.1	5.1	3.5	5.0	5.4	8.8
As obtained ($CO+H_2$) FE%	100.1	100.9	101.9	102.2	103.0	102.5	102.6

Test condition: Measured in CO_2-saturated 0.5 M $KHCO_3$ solution with a catalyst loading of 0.226 mg cm^{-2}.

Table S8. Comparison of TOF over various catalysts in CO_2-saturated 0.5 M $KHCO_3$.

Catalysts	**Metal loading (wt%)**	**Cathode Loading (mg cm^{-2})**	**Potential/ Overpotential [a-b](V)**	**CO Faradaic efficiency (%)**	**CO Current density (mA cm^{-2})**	**TOF (hr^{-1})**	**References**
C-Zn_1Ni_4 ZIF-8	5.44	0.088	-0.63/0.52	94.5	4.7	1059±24	This work
C-Zn_1Ni_4 ZIF-8	5.44	0.088	-0.83/0.72	98.0	22.0	4964± 233	This work
C-Zn_1Ni_4 ZIF-8	5.44	0.088	-0.93/0.82	97.5	31.4	7175± 369	This work
C-Zn_1Ni_4 ZIF-8	5.44	0.088	-1.13/1.02	94.0	44.1	10087± 216	This work
C-Zn_1Ni_1 ZIF-8	2.07	0.226	-1.13/1.02	91.4	40.0	9820± 651	This work
Ni SAs/ N-C	1.53	0.1	-1.0/0.89	70.3	7.37	5273	12
C-AFC ©ZIF-8	1.47	2.0	-0.53/0.42	89.6	4.8	170	13
C-AFC ©ZIF-8	1.47	2.0	-0.83/0.72	78.2	8.1	288	13
COF-367 -Co	--	--	-0.67/0.56	91%	3.3	165 (1908*)	14
COF-367 -Co (1%)	--	--	-0.67/0.56	53%	0.45	764 (9360*)	14
CoFPc	--	--	-0.8/0.69	93%	~4.23	5796	15
CoFPc	--	--	-0.9/0.79	82.1%	~5.2	7380	15

*Calculated on the basis of the amount of electroactive sites.

Table S9. Ni and Zn contents (wt%) of C-Zn$_x$Ni$_y$ ZIF-8 (900ºC-4h) as measured by ICP-OES and derived from XPS analysis.

Sample	**C-Zn$_2$Ni$_1$ ZIF-8 (900ºC-4h)**	**C-Zn$_1$Ni$_1$ ZIF-8 (900ºC-4h)**	**C-Zn$_1$Ni$_4$ ZIF-8 (900ºC-4h)**
Ni wt%-ICP	0.72	1.45	5.03
Zn wt%-ICP	8.43	8.81	6.20
Ni wt%-XPS	0.74	1.45	4.95
Zn wt%-XPS	8.32	8.42	6.11

Table S10. EXAFS data fitting results of C-Zn$_x$Ni$_y$ ZIF-8 (900ºC-4h) for Ni K-edge.

Sample	**Ni-N CN**	**R (Å)**	**σ^2 *10^2 (Å^2)**	**ΔE_0 (eV)**	**R factor**
C-Zn$_2$Ni$_1$ ZIF-8(900ºC-4h)	2.7 ± 0.3	1.86 ± 0.01			
C-Zn$_1$Ni$_1$ ZIF-8(900ºC-4h)	2.7 ± 0.3	1.86 ± 0.01	0.3±0.1	-5.3±0.9	0.1003
C-Zn$_1$Ni$_4$ ZIF-8(900ºC-4h)	2.7 ± 0.2	1.87 ± 0.01			

Table S11. EXAFS data fitting results of C-Zn$_x$Ni$_y$ ZIF-8 (900ºC-4h) for Zn K-edge.

Sample	**Zn-N CN**	**R (Å)**	**σ^2 *10^2 (Å^2)**	**ΔE_0 (eV)**	**R factor**
C-Zn$_2$Ni$_1$ ZIF-8(900ºC-4h)	3.4 ± 0.7	2.02 ± 0.02			
C-Zn$_1$Ni$_1$ ZIF-8(900ºC-4h)	3.6 ± 0.7	2.01 ± 0.02	0.4±0.1	-5.3±2.0	0.022
C-Zn$_1$Ni$_4$ ZIF-8(900ºC-4h)	3.5 ± 0.6	2.02 ± 0.02			

Table S12. The total nitrogen content and percentage of different nitrogen species in C-Zn_xNi_y ZIF-8 (900ºC-4h).

Sample	**C-Zn_2Ni_1 ZIF-8 (900ºC-4h)**	**C-Zn_1Ni_1 ZIF-8 (900ºC-4h)**	**C-Zn_1Ni_4 ZIF-8 (900ºC-4h)**
N wt%	11.37	12.69	10.75
Pyridinic	5.56	6.88	4.22
Metal-N(N-M)	1.68	1.64	2.59
Pyrrolic	2.46	2.69	2.29
Graphitic	1.20	0.94	1.17
N-oxide	0.47	0.54	0.48

Table S13. Porosity characters of C-Zn_xNi_y ZIF-8 (900ºC-4h).

Catalyst	**BET surface area (m^2 g^{-1})**	**Micropore surface area (m^2 g^{-1})**	**External surface area (m^2 g^{-1})**	**V_{total} (cc g^{-1})**	**V_{μ} (cc g^{-1})**
C-Zn_2Ni_1 ZIF-8(900ºC-4h)	892.9	669.5	223.4	1.57	0.28
C-Zn_1Ni_1 ZIF-8(900ºC-4h)	824.4	580.3	244.1	1.61	0.26
C-Zn_1Ni_4 ZIF-8(900ºC-4h)	775.2	518.5	256.7	1.20	0.20

Table S14. Thermodynamic free energy corrections for gas-phase species from DFT calculations. Unit: eV; T = 298K.

Species	**E_{DFT}**	**ZPE**	**∫CvdT**	**TΔS**	**G**
H_2	-6.76	0.29	0.03	0.43	-6.87
H_2O	-14.23	0.59	0.12	0.67	-14.29
CO_2	-22.98	0.31	0.00	0.66	-23.33
CO	-14.79	0.13	0.05	0.67	-15.28

Table S15. Thermodynamic free energy corrections for adsorbates from DFT calculations. Unit: eV; T = 298K.

Species	**ZPE**	**∫CvdT**	**TΔS**	**ΔG**
***COOH**	0.60	0.04	0.07	0.58
***CO**	0.21	0.02	0.03	0.20
***H**	0.18	0.01	0.02	0.17

References:

1. R. Li, X. Ren, X. Feng, X. Li, C. Hu and B. Wang, *Chem. Comm.*, 2014, **50**, 6894-6897.
2. S. Yu, J. Wei, J. Li, Q. Gu, S. Zhang, H. Wang, Y. Ma, N. Li, Q. Gao, R. Si, F. Sun, Y. Wang, F. Song, J. Xu, H. Yu, Y. Zou, Q. Wang, Z. Jiang and Y. Huang, *Nucl. Sci. Tech.*, 2015, **26**, 050102-050106.
3. D. Gao, H. Zhou, J. Wang, S. Miao, F. Yang, G. Wang, J. Wang and X. Bao, *J. Am. Chem. Soc.*, 2015, **137**, 4288-4291.
4. X. Feng, K. Jiang, S. Fan and M. W. Kanan, *J. Am. Chem. Soc.*, 2015, **137**, 4606-4609.
5. S. Yang, Z. X. Huang, X. H. Hou, F. F. Cheng, S. H. Wu and J.J. Sun, Electrochem. Commun., 2016, 68, 71-75.
6. M. R. Singh, E. L. Clark and A. T. Bell, Phys. Chem. Chem. Phys., 2015, 17, 18924-18936.
7. G. Kresse and J. Furthmüller, *Phys. Rev. B*, 1996, **54**, 11169-11186.
8. P. E. Blöchl, *Phys. Rev. B*, 1994, **50**, 17953-17979.
9. J. P. Perdew, K. Burke and M. Ernzerhof, *Phys. Rev. Lett.*, 1996, **77**, 3865-3868.
10. H. J. Monkhorst and J. D. Pack, *Phys. Rev. B*, 1976, **13**, 5188-5192.
11. A. A. Peterson, F. Abild-Pedersen, F. Studt, J. Rossmeisl and J. K. Nørskov, *Energy Environ. Sci.*, 2010, **3**, 1311-1315.
12. C. Zhao, X. Dai, T. Yao, W. Chen, X. Wang, J. Wang, J. Yang, S. Wei, Y. Wu and Y. Li, *J. Am. Chem. Soc.*, 2017, **139**, 8078-8081.
13. Y. Ye, F. Cai, H. Li, H. Wu, G. Wang, Y. Li, S. Miao, S. Xie, R. Si, J. Wang and X. Bao, *Nano Energy*, 2017, **38**, 281-289.
14. S. Lin, C. S. Diercks, Y.-B. Zhang, N. Kornienko, E. M. Nichols, Y. Zhao, A. R. Paris, D. Kim, P. Yang, O. M. Yaghi and C. J. Chang, *Science*, 2015, **349**, 1208-1213.
15. N. Morlanés, K. Takanabe and V. Rodionov, *ACS Catal.*, 2016, **6**, 3092-3095.
16. Q. Lu, J. Rosen, Y. Zhou, G. S. Hutchings, Y. C. Kimmel, J. G. Chen and F. Jiao, *Nat. Commun.*, 2014, **5**, 3242-3248.
17. C. Rogers, W. S. Perkins, G. Veber, T. E. Williams, R. R. Cloke and F. R. Fischer, *J. Am. Chem. Soc.*, 2017, **139**, 4052-4061.
18. D. H. Won, H. Shin, J. Koh, J. Chung, H. S. Lee, H. Kim and S. I. Woo, *Angew. Chem. Int. Ed.*, 2016, **55**, 9297-9300.
19. Y. Hori, A. Murata, K. Kikuchi and S. Suzuki, *J. Chem. Soc.,Chem. Commun*, 1987, 728-729.
20. M. Liu, Y. Pang, B. Zhang, P. De Luna, O. Voznyy, J. Xu, X. Zheng, C. T. Dinh, F. Fan, C. Cao, F. P. de Arquer, T. S. Safaei, A. Mepham, A. Klinkova, E. Kumacheva, T. Filleter, D. Sinton, S. O. Kelley and E. H. Sargent, *Nature*, 2016, **537**, 382-386.
21. P. Su, K. Iwase, S. Nakanishi, K. Hashimoto and K. Kamiya, *Small*, 2016, **12**, 6083-6089.
22. A. S. Varela, N. Ranjbar Sahraie, J. Steinberg, W. Ju, H. S. Oh and P. Strasser, *Angew. Chem. Int. Ed.*, 2015, **54**, 10758-10762.
23. J. Wu, M. Liu, P. P. Sharma, R. M. Yadav, L. Ma, Y. Yang, X. Zou, X. D. Zhou, R. Vajtai, B. I. Yakobson, J. Lou and P. M. Ajayan, *Nano Lett.*, 2016, **16**, 466-470.
24. S. Liu, H. Tao, L. Zeng, Q. Liu, Z. Xu, Q. Liu and J. L. Luo, *J. Am. Chem. Soc.*, 2017, **139**, 2160-2163.